



NRL/MR/6721--93-7317

Numerical Modeling of the Temperature Gradients and Spectra of the Plasma Armature on Thunderbolt

PAUL C. KEPPEL
ROBERT W. CLARK

*Radiation Hydrodynamics Branch
Plasma Physics Division*

June 14, 1993



Approved for public release; distribution unlimited.

93-15106



90

14

REPORT DOCUMENTATION PAGE			Form Approved OMB No. 0704-0188	
Public reporting burden for this collection of information is estimated to average 1 hour per response, including the time for reviewing instructions, searching existing data sources, gathering and maintaining the data needed, and completing and reviewing the collection of information. Send comments regarding this burden estimate or any other aspect of this collection of information, including suggestions for reducing this burden, to Washington Headquarters Services, Directorate for Information Operations and Reports, 1215 Jefferson Davis Highway, Suite 1204, Arlington, VA 22202-4302, and to the Office of Management and Budget, Paperwork Reduction Project (0704-0188), Washington, DC 20503.				
1. AGENCY USE ONLY (Leave Blank)	2. REPORT DATE June 14, 1993	3. REPORT TYPE AND DATES COVERED Memorandum		
4. TITLE AND SUBTITLE Numerical Modeling of the Temperature Gradients and Spectra of the Plasma Armature on Thunderbolt			5. FUNDING NUMBERS PE - 63220C	
6. AUTHOR(S) Paul C. Kepple and Robert W. Clark				
7. PERFORMING ORGANIZATION NAME(S) AND ADDRESS(ES) Naval Research Laboratory Washington, DC 20375-5320			8. PERFORMING ORGANIZATION REPORT NUMBER NRL/MR/6721-93-7317	
9. SPONSORING/MONITORING AGENCY NAME(S) AND ADDRESS(ES) Strategic Defense Initiative Organization T/IS, Pentagon Washington, DC 20301-7100			10. SPONSORING/MONITORING AGENCY REPORT NUMBER	
11. SUPPLEMENTARY NOTES This work was supported by the Strategic Defense Initiative Organization under Job Title, Ultra Short Wavelength Laser Research.				
12a. DISTRIBUTION/AVAILABILITY STATEMENT Approved for public release; distribution unlimited.			12b. DISTRIBUTION CODE	
13. ABSTRACT (Maximum 200 words) Numerical simulations of the spectra recorded on Thunderbolt shots 26 and 27 are presented. The calculations proceed via multifrequency radiation transport and are based on the assumptions that the plasma armature is cylindrically symmetric, the atomic constituents are homogeneously mixed and in pressure equilibrium, and the temperature gradient is specified by $T(r_i) = T_c(1.0 - r_i/r_w)^a$. For the case of shot 27 the simulation is in excellent agreement with experiment and leads to a specific inference of a temperature gradient. For the case of shot 26 (where one capacitor bank fired early) the simulations indicate that the plasma armature for this shot did not satisfy some or all of the assumptions above. Since the aluminum absorption feature on shot 26 is too narrow relative to the B II and Cu I features there probably was a "blob" of aluminum near the wall.				
14. SUBJECT TERMS Rail gun Numerical Modeling Diagnostics			15. NUMBER OF PAGES 39	
			16. PRICE CODE	
17. SECURITY CLASSIFICATION OF REPORT UNCLASSIFIED	18. SECURITY CLASSIFICATION OF THIS PAGE UNCLASSIFIED	19. SECURITY CLASSIFICATION OF ABSTRACT UNCLASSIFIED	20. LIMITATION OF ABSTRACT UL	

CONTENTS

INTRODUCTION	1
COMPUTER CODE AND ATOMIC DATA	2
RESULTS OF FITTING OBSERVED SPECTRA	6
CONCLUSIONS	10
FUTURE WORK	11
ACKNOWLEDGEMENTS	11
REFERENCES	12

DTIC QUALITY ASSURANCE

Accession For	
NTIS GRA&I	<input checked="" type="checkbox"/>
DTIC TAB	<input type="checkbox"/>
Unannounced	<input type="checkbox"/>
Justification	
By	
Distribution/	
Availability Codes	
Avail and/or	
Dist	
A-1	

NUMERICAL MODELING OF THE TEMPERATURE GRADIENTS AND SPECTRA OF THE PLASMA ARMATURE ON THUNDERBOLT

INTRODUCTION

The purpose of this work is to demonstrate how, via numerical modeling of spectra, one can infer some information about the hot interior of a dense plasma from the radiation which is emitted principally by the optically thick cold exterior. The experimental data for this work are two spectra recorded by Dennis Keefer and his group from the University of Tennessee Space Institute from shots 26 and 27 of the Thunderbolt facility operated by the Westinghouse group headed by Hugh Calvin.

Thunderbolt is an "experimental test bed" rail gun. The features that are important for this work are shown in Fig. 1. The inner part of the Thunderbolt barrel consists of alternate sectors of copper rail and boron nitride (BN) insulator. The projectile is injected into Thunderbolt at a relatively high velocity by a light gas gun. When the projectile is well into the barrel a large voltage is induced between the rails and an arc is drawn through an aluminum fuse attached to the back of the projectile. The arc ionizes the fuse and some of the gas thus creating a "plasma armature". The $\mathbf{J} \times \mathbf{B}$ force on the armature further accelerates the projectile. By the time the projectile is several meters into the barrel, the plasma armature contains, in addition to the aluminum from the fuse, a significant component

of copper, boron, and nitrogen. These constituents of the armature are continuously ablated from the rails and insulators. Thus the set of atomic elements that need to be included in the modeling are: aluminum, boron, copper, and nitrogen. The states included in the atomic data table are listed in Table I.

The spectra were recorded via an optical fiber inserted through a radial hole in the insulator (BN). The experimental set up is similar to that described by Sedghinasab, Keefer, and Crowdr¹ and Keefer and Crawford². The optical fiber used has a band pass window of 295 - 345 nm. Although neither B I or N I have any strong lines in the spectral window imposed by the optical fiber, there are reasons for their inclusion in the atomic data base. Boron and nitrogen must be included in order to calculate accurate opacities. B I has strong lines just outside the window at 209 and 250 nm which are important for energy transport and wall loading. Finally, there is a weak B II line, $2s2p^1P - 2p^2^1D$ at 345.1 nm, just outside the optical fiber window. The high energy wing of this line is in the window and since the lower level of this line is an excited state, the opacity in the line should be small enough for the wing to be present in emission. The intensity and width (slope of the wing) should be a valuable diagnostic of the internal temperature and density. As an extension of this temperature diagnostic a list of the strong lines in the optical fiber window (OFW) from elements that might be included (seeded) in the plasma armature is included as Table II. In this table the first quantity is the wavelength of the line in Angstroms, the second is the relative strength of the line in arbitrary units, and the third is the emitting atom or ion. An inspection of this table reveals several elements (Ni and V to name two) that have lines from the neutral and first ionized ions that are well removed from the strong Cu I and Al I lines and thus could be valuable diagnostic additions.

COMPUTER CODE AND ATOMIC DATA

The ionic populations in the plasma may be characterized by a set of atomic rate equations of the form

$$\frac{\delta f_{ikm}}{\delta t} = \sum_j \left(w_{jikm} f_{jkm} - w_{ijkm} f_{ikm} \right),$$

where f_{ikm} is the fractional population of atomic level i for species m in spatial zone k , and w_{jikm} is the net rate describing the transition from initial state j to final state i . An equation

of this type is constructed for each of the atomic levels included in the model. In the present instance, the assumption of collisional-radiative equilibrium (CRE) is made, which involves dropping the explicit time dependence in the above equation. The rate coefficients that are used to calculate the populating and depopulating rates, W_{jikm} , are calculated using various scattering techniques and the methods used in calculating the corresponding rate coefficients are summarized elsewhere³.

Radiation emission from the plasma and its opacity are dependent on the local atomic-level population densities. Except for optically thin plasmas, however, the level populations depend on the radiation field, since optical pumping via photoionization and photoexcitation can produce significant population redistribution. Thus, the ionization and radiation transport processes are strongly coupled and must be solved self-consistently. In this model, an iterative⁴ procedure is used, where level populations are calculated using the radiation field from the previous iteration, then using these populations to calculate a new radiation field until convergence is reached.

The equation of radiative transport is solved at a large number of discrete frequencies, providing resolution of emission lines, recombination edges and absorption edges. At each frequency ν and spatial zone k , contributions to the total opacity $k_{\nu k}$ and emission coefficient $j_{\nu k}$ from each bound-bound, bound-free and free-free process are summed. For example, the contributions from the bound-bound transition $i-i'$ of material m to $k_{\nu k}$ and $j_{\nu k}$ are given by

$$k_{\nu k}^{ii'm} = f_{ikm} n_{km} u_{vii'm} A_{ii'm} \frac{h^2 c^2}{2 E_{ii'm}^2 g_{im}} \left(1 - \frac{f_{i'km} g_{im}}{f_{ikm} g_{i'm}} \right),$$

and

$$j_{\nu k}^{ii'm} = f_{i'km} n_{km} u_{vii'm} A_{ii'm} E_{ii'm},$$

respectively. The factor in brackets represents the reduction in opacity due to stimulated emission. n_{km} is the ion density in zone k . $E_{ii'm}$ is the transition energy, g_{im} is the statistical weight, $A_{ii'm}$ is the radiative decay rate and $u_{vii'm}$ is the line profile function. Voigt line profiles were used in the present calculation. Similarly, the contributions to $k_{\nu k}$ and $j_{\nu k}$ from the free-bound (radiative recombination) process for atomic level i of material m are

$$k_{\nu k}^{im\infty} = f_{ikm} n_{km} \sigma_{im} \frac{E_{im\infty}^3}{h^3 \nu^3} \left[1 - \frac{f_{ikm}^{\infty} g_{im} n_k}{f_{ikm} g_{im}^{\infty} \beta_0} T_k^{-3/2} e^{[E_{im\infty} - h\nu]/kT_k} \right],$$

$$j_{\nu k}^{im\infty} = f_{ikm}^{\infty} n_{km} \sigma_{im} \frac{2 E_{im\infty}^3}{h^2 c^2} \frac{g_{im} n_k}{g_{im}^{\infty} \beta_0} T_k^{-3/2} e^{[E_{im\infty} - h\nu]/kT_k},$$

for $h\nu \geq E_{im\infty}$. The factor in brackets represents the reduction in opacity due to stimulated recombination. T_k and n_k are the local electron temperature and electron density. $E_{im\infty}$ is the ionization energy, σ_{im} is the photoionization cross section and $\beta_0 = (1/2)h^3/(2\pi m_e k)^{3/2}$. Finally, the contributions to $k_{\nu k}$ and $j_{\nu k}$ from free-free (Bremsstrahlung) processes are given by

$$k_{\nu k}^{ff} = C_{ff} \frac{\langle z_k^2 \rangle n_k}{\sqrt{T_k}} G_{\nu} \frac{1}{h\nu^3} \left[1 - e^{-h\nu/kT_k} \right],$$

$$j_{\nu k}^{ff} = C_{ff} \frac{\langle z_k^2 \rangle n_k}{\sqrt{T_k}} G_{\nu} \frac{2}{c^2} e^{-h\nu/kT_k},$$

where $C_{ff} = 8\pi e^6/[3m_e c(6\pi m_e k)^{1/2}]$, $\langle z_k^2 \rangle$ is the mean square of the ionization and G_{ν} is the Gaunt factor.

When the plasma is optically thick at a particular frequency ν , the emitted intensity will be given j_{ν}/k_{ν} . If the plasma is in local thermodynamic equilibrium (LTE), the intensity will reduce to the Planck radiation field at that frequency. In LTE, the atomic populations satisfy the Boltzmann-Saha relations

$$\frac{f_{i'km} g_{im}}{f_{ikm} g_{i'm}} = e^{-E_{ii'm}/kT_k}$$

and

$$\frac{f_{ikm}^{\infty} g_{im} n_k}{f_{ikm} g_{im}^{\infty} \beta_0} T_k^{-3/2} = e^{-E_{im\infty}/kT_k}$$

Then the ratios $j_{vk}^{ii'm}/k_{vk}^{ii'm}$, $j_{vk}^{im\infty}/k_v^{im\infty}$, and j_v^{ff}/k_{vk}^{ff} independently reduce to

$$\frac{j_v}{k_v} = \frac{2}{c} \frac{h\nu^3}{e^{\frac{h\nu}{kT}} - 1} = B_\nu$$

which is the Planck intensity.

The radiative couplings $C_{vkk'}$ to each of the other zones k' are subsequently calculated from the opacities and the optical paths described by the geometry of the problem. The method of obtaining angle-averaged escape probabilities in cylindrical and spherical geometries is explained in reference⁵. The local rate of energy density change in zone k due to radiation transport is then given by

$$\frac{\partial E_k}{\partial t} = \sum_n \left[-j_{vk} + \sum_{k'} C_{vk'k} j_{vk'} \right] \delta\nu,$$

and the photoexcitation rate for the transition $i-i'$ is

$$W_{ii'mk} = \sum_v \frac{k_{vk}^{ii'm}}{k_{vk}} \sum_{k' \neq k} \left[C_{vk'k} j_{vk'} V_{k'} \right] \frac{\delta\nu}{n_{km} f_{ikm} E_{ii'm} V_k},$$

where $k_{vk}^{ii'm}$ is the opacity for the bound-bound process $i-i'$ defined above. Similarly, the photoionization rate for level i of material m is

$$W_{imk\infty} = \sum_v \frac{k_{vk}^{im\infty}}{k_{vk}} \sum_{k' \neq k} \left[C_{vk'k} j_{vk'} V_{k'} \right] \frac{\delta\nu}{n_{km} f_{ikm\infty} E_{im\infty} V_k},$$

where $k_{vk}^{ii'm}$ is the opacity for the bound-free process (the ionization of atomic level i) and V_k is the volume of zone k .

For each state included in the modeling, Table I includes the energy level of the state, its statistical weight, and designation or name. The energy levels and transition probabilities of ionic states were obtained from Cowan's code⁶. For atoms (neutrals), configuration interaction is important enough that it is more difficult to get accurate energy levels from Cowan's code. On the other hand some data is in the literature, therefore, the energy levels and transition probabilities for the states of B I and N I were obtained from Wiese, Smith, and Glennon⁷, for the states of Al I the source was Wiese, Smith, and Miles⁸. The data for Cu I was obtained from references 9 - 15. The collisional ionization rates were calculated using a semiclassical approximation described in reference 16. The photoionization cross sections were calculated as described in reference 16 using the Karzes and Latter¹⁷ Gaunt factors. For dipole allowed transitions the collisional excitation rates were calculated using the semiclassical approximation summarized in reference 16. The distorted wave code developed by M. Blaha¹⁸ was used for the monopole and quadrupole excitation rates. The Blaha's distorted wave with exchange code¹⁸ was used for those spin-flip collisional excitations that were included.

RESULTS OF FITTING OBSERVED SPECTRA

The spectra recorded on Thunderbolt shots 26 and 27 are shown in Figures 2 and 3. The task of the work reported here is to numerically simulate these spectra. There are three dominant features in the experimental spectra. Starting at 3.6 eV is the wing of the B II $2s2p\ ^1P - 2p^2\ ^1D$ mentioned above. Centered at 3.8 eV is a (partial) blend of two Cu I lines: $4p\ ^2D_{1/2} - 4s\ ^2S_{1/2}$ and $4p\ ^2D_{3/2} - 4s\ ^2S_{1/2}$. The third major feature is at about 4.1 eV and is a blend of two Al I lines. These two lines have a common upper level and terminate on the two components of the Al I ground state. These two components are separated by only 0.01 eV and are treated as a single state in the model. Thus in the synthetic spectrum the aluminum feature is modeled as a single line: $3d\ ^2D - 3p\ ^2P$. This latter line is strongly quenched by electron collisions that excite the upper level from the 3d to the 4p level. The 3d and 4p levels are only 0.065 eV apart and the collision is dipole allowed so the collision rate is large. For $T_e = 2$ eV, the rate coefficient is nearly 10^{-5} cm³/sec! This strong quenching results in a very broad line. The strongest quenching of the two Cu I lines results from electron collisions that transfer the excitation back and forth between the upper levels of the two lines. The upper levels of these two lines are only 0.03 eV apart, but the transitions are not dipole allowed and thus the excitation rate coefficient at $T_e = 2$ eV is almost an order of magnitude smaller than for the rate that quenched the Al I line. Thus the width of the Cu I lines is much smaller than the Al I line. These line widths are demonstrated in Fig. 4, the

spectrum of an optically thin, homogeneous plasma with: $T_e = 1$ eV, $P = 3 \times 10^8$ dynes/cm², and equal numbers of aluminum, copper, boron, and nitrogen atoms or ions. The dashed curve superimposed on Fig 4 is a 1 eV black body for comparison. The small dip in the center of the Al I line profile is a construct or artifact in the program. It is the result of an interaction between frequency gridding and the overlapping of lines, edges etc. Figure 5 shows the spectrum when $T_e = 2$ eV and the plasma consists of .2% Al, 20% Cu, and 80% BN (% by mass). At 2 eV Al I is virtually absent and Cu I is reduced to the point where the wing of the B II line (starting at 3.6 eV) now dominates the spectrum in the OFW. Figures 4 and 5 show the intrinsic line shapes and widths at temperatures and densities characteristic of the bulk of the plasma armature. In the remaining synthetic spectra shown in this report the effects of opacity, radiation transport and gradients in temperature and density are combined with these intrinsic profiles to produce the synthetic spectra.

A number of calculations were made with a multifrequency radiation transport code using aluminum, copper, boron, and nitrogen atomic data. These runs were made to scope out the composition of the plasma and the temperature and density profiles. In these runs the adjustable parameters were: a) the fraction (by mass) of aluminum and copper (the remainder is BN), b) the electron temperature on axis (in eV), c) the partial pressure (dynes/cm², of the four constituents we model, and d) α , the exponent in the electron temperature profile equation suggested by Schlichting¹⁹ on the basis of an analogy to the velocity profile in turbulent flow, and used by Tidman, Goldstein, and Windsor²⁰ for a plasma armature:

$$T(r_i) = T_c (1.0 - r_i/r_w)^\alpha.$$

where r_i is the radius to the center of the i th cell and $r_w = 2.8$ cm is the radius of the wall. Most of the runs in this set used 30 radial cells and a common radial grid. In order to resolve the temperature gradient on the outside, the cell spacing decreased with radius. In Fig. 6 the temperature profiles for a temperature on axis of 2 eV and $\alpha = 1/4$ (o o o), $1/6$ (* * *), $1/8$ (+ + +), and $1/10$ (x x x) are plotted. Note that, for the radial grid used, the temperature gradient is well resolved and the temperature in the 30 th cell is small.

Since there are only three spectral features plus the continuum, one might suspect that a unique fit may be "too much to hope for". In addition the modeling is complicated by the fact that the experimental spectra were time integrated, and that the plasma armatures may not be perfectly cylindrically symmetric and homogeneous as we assume in the numerical modeling. Although at this stage we will see how far we can go without them, time resolved spectroscopy and absolute calibration of the spectrometer may be possible and would ease the modeling task considerably.

The opacity in the vicinity of the aluminum line is typically dominated by the continuum, thus the width of the aluminum line is, to first approximation, controlled by the total mass density or pressure. With this observation one can fix the pressure from the linewidth at about 3×10^8 dynes/cm². Next one notes that in the measured spectra the copper absorption feature does not extend to the base line. A value of α of about 1/10 is required to accurately simulate this feature of the spectra. (It should be noted again that we assume a homogeneous plasma with cylindrical symmetry in the density and temperature, a few warm spots near the outside wall in the actual plasma could easily lead us to assign too small a value to α .) As indicated, the best fit of the numerical spectrum to that of Thunderbolt 27 was achieved with: $T_c = 2$ eV, $P = 3 \times 10^8$ dynes/cm², $\alpha = 1/10$, 0.2% Al, 20% Cu, and 79.8% BN. This spectrum is shown in Fig. 7 and 8. Figure 7 is limited to the OFW and is a linear plot. Figure 8 is a survey plot with the energy range extended to 1 - 10 eV and the intensity is logarithmic. Superimposed on this survey plot is the spectrum corresponding to a black-body at the central temperature, T_c . The survey plot, which clearly shows the deviation from black body, is useful for estimates of wall loading and radiative cooling. Also included as Fig. 9 is the plot of the optical depth. The dashed curve on Fig. 9 is the free-free contribution to the opacity. From Fig. 9 one should note that while the two copper lines have optical depth of more than 1000, the wing of the B II line over 600, even the bound-free continuum has optical depth of 100! Figs. 10 and 11 show the accessibility as viewed from the outside (labeled "Front") and from the center (labeled "Back"). The accessibility is defined as the fraction of the radius to the point of unity optical depth. Thus the outside ("Front") accessibility is useful in determining the origin of the radiation that impinges on the wall and is limited to the OFW, while the center ("Back") accessibility is useful in estimating the energy transported by radiation from the hot interior outward and is plotted over the 1 - 10 eV range.

Inspection of the back accessibility, Fig. 11, reveals that even the continuum radiation penetrates at most 1% of the way out of the cylinder. In view of this fact one might question the sensitivity of the emitted spectrum to the details of the temperature profile at the center. To investigate this sensitivity two runs were made using the same parameters as the previous run but with a spike (dip) in the temperature at the center. The spike had a magnitude of 2 eV and an extent of 0.5 cm. The dip had a magnitude of 1 eV and the same extent. The spectra in the OFW of these two runs were indistinguishable from that of the previous run (Fig. 7). Thus, to nobody's great surprise, one concludes that the emitted spectrum is not sensitive to the details of the temperature in the innermost 20 - 30 % of the plasma! Rather than proceed with a set of runs with temperature distributions modified over larger and larger portions of the central region, let us investigate the sensitivity of the emitted spectra to other parameters.

Figure 12 shows the spectrum in the OFW for the case with $T_c = 3$ eV and the other parameters unchanged from above. Note that unlike the case described above, the plasma for the present case is 50 % hotter everywhere than that for Fig. 7. For Fig. 13 $T_c = 2$ eV but $P = 4 \times 10^8$ dynes/cm². For Fig. 14 $T_c = 3$ eV and $P = 4 \times 10^8$ dynes/cm². The sensitivity of the spectra to T_c and P is evident from the comparison of Fig. 7 to Figs. 12-14. The sensitivity of the spectra to α , the coefficient in the temperature distribution equation is evident from the comparison of Fig. 7 to Figs. 15 and 16. For Fig. 7 $\alpha = 1/10$, for Figs. 15 and 16 $\alpha = 1/8$ and $1/6$ respectively. The sensitivity is evident! Although the figures are not included, the sensitivity analysis on the composition has been performed. The synthetic spectrum is measurably different when the composition of either aluminum or copper is changed by 25 per cent.

The radial gridding on all runs to this point was the same. In order to resolve the temperature gradient, the cell size decreased with r . The grid consists of 30 cells, with the cell size decreasing as a geometric progression. The 30-th cell goes from $r = 2.79991$ to $r = 2.80000$ cm so that the cell is 9×10^{-5} cm thick. An inspection of Fig. 10, the Front Accessibility shows that, at line center of the copper features, the accessibility is 5×10^{-6} . Thus the photons that strike the wall come from a layer 1.4×10^{-5} cm thick and our last cell is optically thick at line center! Since it was just these line centers that were used to fix α , a run was made using a radial grid that reduced the maximum opacity through the outer cell to 1. The other parameters for this run were those of Fig. 7. Comparison of this run shown in Fig. 17 to Fig. 7 shows that perhaps we should assign some uncertainty to α . The cell sizes are so small that use of the Schlichting-Tidman equation for temperature has to be questioned. One may need a wall loading, sputtering etc model coupled to thermal conduction and (turbulent?) hydrodynamic to assign a temperature that close to the wall. To follow that trend for a bit more, a couple of runs were made in which there is a thin layer near the wall with no copper or aluminum. The layer thickness was 1 mm and 0.07 mm the resulting spectra are shown in Figs. 18 and 19 respectively. Figure 18 shows the copper lines weakly in emission, thus a layer 1 mm thick is ruled out. Figure 19, although very different from Fig. 7, can not yet be used to rule out a 0.07 mm unmixed layer. The question is: are there parameters (α , P , T_c , etc) that, when used with that unmixed layer still yield a synthetic spectrum that matches Fig. 3? To pursue that question, two more runs were made. Figure 20 shows the effect of changing α to $1/6$, and is clearly a step in the right direction. Figure 21 shows the additional effect of reducing the pressure to 1.0×10^8 dynes/cm². Although the synthetic spectrum in Fig. 21 is now getting close to that of Thunderbolt shot 27, that low a pressure can be ruled out on the basis of other diagnostics, thus one can state that if there is a layer near the wall where the (turbulent?) mixing is not effective, it is clearly thinner than 0.07 mm!

After an extensive search of parameter space, none were found such that the numerical spectra matched that measured on Thunderbolt shot 26. The aluminum absorption feature in the measured spectra is too narrow compared to the copper features. From the above negative results we infer that the plasma armature on shot 26 did not satisfy some of the assumptions, probably that of homogeneous mixing.

CONCLUSIONS

For shot 27: The spectroscopy is consistent with the assumptions of cylindrical symmetry, homogeneous mixing of the atomic constituents, pressure equilibrium, and a very strong temperature/density gradient at the outside edge. For a radial temperature distribution given by equation 1, the spectrum is consistent with an α of $1/10 - 1/8$ and $T_c = 2$ eV. Further, the spectra is consistent with $P = 3 \times 10^8$ dynes/cm², a plasma armature consisting of 20% copper, 0.2% aluminum, and the remainder BN. If there is an unmixed boundary layer, its thickness is smaller than 0.007 cm. Although the spectral analysis can not rule out a central spike or dip in the temperature, the requirement of homogeneous mixing and strong temperature gradient on the outside render it most unlikely.

For shot 26: One capacitor back fired early on this shot, thus one would not be surprised if the plasma armature were pathological in some way. From the narrowness of the aluminum feature compared to those of copper, one is lead to the conclusion that the spectrum on shot 26 is not consistent with some or all of the assumptions: cylindrical symmetry, homogeneous mixing of the atomic constituents, pressure equilibrium, and radial temperature distribution such as equation 1. Since the Cu I and B II features are similar to those on shot 27, it is the assumption of homogeneous mixing that is most likely violated. (i.e. a "blob" of aluminum near the wall).

Fundamental Physics: The absorption features are sensitive to the temperature gradient. Thus to some extent one of the quantities critical to the understanding of the plasma armature, i.e. the temperature gradient, can be inferred from spectroscopy. The sensitivity of the spectrum to unmixed boundary layers is an indication of the strength of the turbulence in the hydrodynamics.

FUTURE WORK

Numerical modeling of the spectra would be enhanced if: a) the experimental spectra were time resolved, b) the instrument were absolutely calibrated, c) the optical fiber had a larger band pass, d) the plasma were seeded with elements that provide additional spectral features (in the OFW), e) spectra were recorded with the optical fiber passing through the rail rather than the insulator. The first three are difficult, the last two much less so. On the theoretical/numerical side: a) a better temperature distribution, at least very near the wall, b) multi-dimensional calculations.

ACKNOWLEDGEMENTS

The authors would like to thank: Dennis Keefer for introducing us to the spectroscopy of plasma armatures and providing the experimental spectra. Hugh Calvin for Figure 1 and permission to use the data from Thunderbolt before publication. Michael Huebschman, John Apruzese, and John Giuliani for many productive discussions. This work was supported by SDIO/TIS.

REFERENCES

1. A. Sedghinasab, D. Keefer, and H. Crowder, IEEE Transactions on Plasma Science 17, 360 (1989).
2. D. Keefer and R. Crwford, IEEE Transactions on Magnetics 25, 295 (1989).
3. D. Duston, R. W. Clark, J. Davis and J. P. Apruzese, Phys. Rev. A 27, 1441 (1983).
4. J. P. Apruzese, J. Davis, D. Duston and R. W. Clark, Phys. Rev. A 29, 246 (1984).
5. J. P. Apruzese, J. Quant. Spectrosc. Radiat. Transf. 25, 419 (1981).
6. R.D. Cowan, "The Theory of Atomic Structure and Spectra", (University of California Press, Berkeley, CA. 1981).
7. W. L. Wiese, M. W. Smith, and B. M. Glennon, "Atomic Transition Probabilities, Hydrogen through Neon". U.S.Department of Commerce, National Bureau of Standards. NSRDS-NBS 4 Vol I.
8. W. L. Wiese, M. W. Smith, and B. M. Miles, "Atomic Transition Probabilities, Sodium through Calcium". U.S.Department of Commerce, National Bureau of Standards. NSRDS-NBS 22 Vol II.
9. C. H. Corliss, J. Res. Nat. Bur. Stand., 66A , 497 (1962).
10. C. H. Corliss, J. Res. Nat. Bur. Stand., 74A, 781 (1970).
11. A. Bielski, J. Quant. Spectrosc. Radiat. Transfer, 15, 463 (1975).
12. F. Zettl, T. Neger, and H. Jaeger, J. Phys. B 17, 1755, (1984).
13. J. Carlsson, Phys. Rev. A 38, 1702 (1988).
14. A. Kono and S. Hattori, J. Quant. Spectrosc. Radiat. Transfer 28, 383 (1982).
15. A. Z. Msezane and R. Henry, Phys. Rev. Lett. 55, 2277 (1985).

- 16 D. Duston and J. Davis, Phys. Rev. A 23, 2602 (1981).
- 17 W.J. Karzas and B. Latter, Astrophys. J. Suppl. Ser. 6, 167 (1961).
- 18 J. Davis, P. Kepple, and M. Blaha, J. Quant. Spectrosc. Radiat. Transfer. 16, 1043 (1976).
- 19 H. Schlichting, Boundary Layer Theory, 6th Edition translated by J. Kestin, McGraw Hill, 1968. See page 707 and following.
- 20 D. A. Tidman, S. A. Goldstein, and N. K. Windsor, IEEE Transactions on Magnetism, 22, 1763 (1986).

Table I
Atomic Structure

AL I			B I		
0.0000	6.0	3p ² P	0.0000	6.0	2p ² P
3.1427	2.0	4s ² S	3.3959	12.0	2s 2p ² ⁴ P
4.0215	10.0	3d ² D	6.2998	10.0	2s 2p ² ² D
4.0867	6.0	4p ² P	7.2436	18.0	n=3
4.7528	30.0	3s 3p ²	7.8667	2.0	2s 2p ² ² S
4.8270	10.0	4d ² D	8.2794	32.0	n=4
5.1229	14.0	4f ² F			
5.8103	50.0	n=5			
AL II			B II		
0.0000	1.0	3s ² ¹ S	0.0000	1.0	2s ² ¹ S
5.1091	12.0	3s 3p	4.6841	9.0	2s 2p ³ P
11.4262	4.0	3s 4s	9.0975	3.0	2s 2p ¹ P
11.4724	15.0	3p ²	12.2611	9.0	2p ² ³ P
12.2336	20.0	3s 3d	12.6877	5.0	2p ² ¹ D
13.1661	12.0	3s 4p	15.8236	1.0	2p ² ¹ S
15.2718	20.0	3s 4d	18.3550	27.0	2s n=3 Trip.
15.3727	28.0	3s 4f	18.8119	9.0	2s n=3 Sing.
16.4999	100.0	3s n=5	21.8616	48.0	2s n=4 Trip.
18.2843	60.0	3p 3d	21.9270	16.0	2s n=4 Sing.
AL III			B III		
0.0000	2.0	3s ² S	0.0000	2.0	2s ² S
6.9138	6.0	3p ² P	6.0084	6.0	2p ² P
14.6741	10.0	3d ² D	22.6171	2.0	3s ² S
16.0579	2.0	4s ² S	24.2037	6.0	3p ² P
18.2215	6.0	4p ² P	24.5888	10.0	3d ² D
20.9485	10.0	4d ² D	30.5077	32.0	n=4
21.1869	14.0	4f ² F	33.3282	50.0	n=5
23.6710	50.0	n=5	34.8438	72.0	n=6

Table I
Continued

Cu I			N I		
0.0000	2.0	4s $^2S_{1/2}$	0.0000	4.0	2p3 4S
1.3890	6.0	4s ² $^2D_{5/2}$	2.2435	10.0	2p3 2D
1.6421	4.0	4s ² $^2D_{3/2}$	3.1185	6.0	2p3 2P
3.7858	2.0	4p $^2P_{1/2}$	10.2499	12.0	2p2 3s 4P
3.8166	4.0	4p $^2P_{3/2}$	11.6727	36.0	2p2 3p Quart.
4.8376	6.0	4p' $^4P_{5/2}$	11.8199	18.0	2p2 3s Doub.
4.9734	4.0	4p' $^4P_{3/2}$	12.8907	60.0	2p2 3d Quart.
5.0763	2.0	4p' $^4P_{1/2}$	13.2904	54.0	2p2 3p Doub.
5.1226	28.0	4p' 4F	13.9866	80.0	2p2 3d Doub.
5.4212	6.0	4p' $^2F_{5/2}$			
5.4710	20.0	4p' 4D	N II		
5.6780	24.0	4p' Doub.	0.0000	9.0	2p2 3P
6.1915	10.0	4d 2D	1.9571	5.0	2p2 1D
6.9763	82.0	Comp.	4.8372	1.0	2p2 1S
			5.1401	5.0	2s 2p3 5S
			11.4279	15.0	2s 2p3 3D
Cu II			13.3628	9.0	2s 2p3 3P
0.0000	1.0	3d ¹⁰ 1S	18.7515	9.0	2p 3s 3P
1.5723	20.0	3d ⁹ 4s	18.9172	3.0	2p 3s 1P
7.1048	60.0	3d ⁹ 4p	21.1874	27.0	2p 3p Trip.
12.6703	100.0	3d ⁹ 4d	21.7307	9.0	2p 3s Sing.
15.1924	140.0	3d ⁹ 4f	23.4969	45.0	2p 3d Trip.
15.6707	500.0	3d ⁹ n=5	23.6856	15.0	2p 3d Sing.
Cu III			N III		
0.0000	10.0	3d ⁹ 2D	0.0000	6.0	2p1 2P
8.3973	90.0	3d ⁸ 4s	6.9489	12.0	2s 2p2 4P
15.6580	270.0	3d ⁸ 4p	12.6293	10.0	2s 2p2 2D
24.4489	450.0	3d ⁸ 4d	15.8204	2.0	2s 2p2 2S
29.3734	630.0	3d ⁸ 4f	18.0952	6.0	2s 2p2 2P
30.8199	2250.	3d ⁸ n=5	23.0657	4.0	2p3 4S
			33.1757	18.0	n=3
			40.8735	32.0	n=4

Table II
Strong Lines in the
Optical Fiber Window

2956.13	1600	Ti I	3134.11	2900	Ni I	3340.34	1100	Ti II
2977.13	1000	Na II	3135.48	2500	Na II	3341.88	5700	Ti I
2980.63	1100	Na II	3137.86	1700	Na II	3349.04	4300	Ti II
2983.570	1000	Fe I	3149.28	2000	Na II	3349.41	2000	Ti II
2986.00	1500	Cr I	3158.16	6000	Mo I	3353.35	2500	Cl II
2986.47	2100	Cr I	3162.57	1000	Ti II	3354.64	4100	Ti I
2989.03	2800	Bi I	3163.74	2000	Na II	3358.12	1600	Mo I
2994.427	1000	Fe I	3168.52	1600	Ti II	3361.21	7200	Ti II
2994.46	1000	Ni I	3170.35	8700	Mo I	3369.57	2900	Ni I
3000.89	1100	Cr I	3179.06	1000	Na II	3370.44	1100	Ti I
3002.49	4000	Ni I	3183.41	3200	V I	3371.45	4300	Ti I
3003.63	2200	Ni I	3183.98	5300	V I	3372.80	5700	Ti II
3012.00	3700	Ni I	3185.40	3800	V I	3377.48	2900	Ti I
3017.57	2800	Cr I	3186.45	2400	Ti I	3380.28	1400	Ti II
3020.639	1500	Fe I	3189.79	1700	Na II	3380.57	3300	Ni I
3021.56	2800	Cr I	3190.87	1000	Ti II	3382.89	28000	Ag I
3024.35	1100	Cr I	3191.99	3100	Ti I	3383.76	5700	Ti II
3024.64	2400	Bi I	3193.97	7600	Mo I	3384.62	1900	Mo I
3037.94	1700	Ni I	3199.92	3800	Ti I	3385.95	1400	Ti I
3044.00	3100	Co I	3208.83	3000	Mo I	3387.84	1400	Ti II
3050.82	3500	Ni I	3212.19	1600	Na II	3388.17	1100	Co I
3054.32	1500	Ni I	3217.06	1100	Ti II	3391.05	1300	Ni I
3056.33	1200	V I	3222.84	1300	Ti II	3392.99	3300	Ni I
3059.086	1000	Fe I	3233.14	1100	Mo I	3394.58	1100	Ti II
3060.46	1400	V I	3234.52	6600	Ti II	3395.38	2200	Co I
3061.82	1700	Co I	3236.57	5200	Ti II	3405.12	11000	Co I
3066.22	1300	Ti II	3239.04	4100	Ti II	3405.94	1300	Mo I
3066.38	2400	V I	3248.60	1200	Ti II	3409.18	4500	Co I
3067.72	9000	Bi I	3252.91	1200	Ti II	3414.76	8200	Ni I
3071.32	1300	Cl II	3254.25	1200	Ti II	3417.16	2700	Co I
3072.97	1100	Ti II	3257.96	1500	Na II	3423.71	1600	Ni I
3075.22	1600	Ti II	3261.60	1200	Ti II	3431.58	2500	Co I
3078.64	2300	Ti II	3267.70	1100	V II	3433.04	4500	Co I
3088.02	3600	Ti II	3280.68	55000	Ag I.	3433.56	2600	Ni I
3101.55	2600	Ni I	3285.60	1700	Na II	3440.606	6000	Fe I
3101.88	1300	Ni I	3289.02	1100	Mo I	3440.989	2500	Fe I
3102.30	3000	V II	3301.35	1700	Na II	3442.93	1600	Co I
3110.71	2600	V II	3304.96	1500	Na II	3443.64	8800	Co I
3112.12	1400	Mo I	3315.43	1900	Cl II	3443.8765	1000	Fe I
3118.38	2000	V II	3318.04	1000	Na II	3446.26	4800	Ni I
3122.78	1600	Au I	3322.94	2900	Ti II	3447.12	3200	Mo I
3123.72	1200	Cl II	3329.10	1200	Cl II	3449.17	4100	Co I
3124.42	1700	Na II	3329.46	2100	Ti II	3453.50	2100	Co I
3125.28	1500	V II	3331.88	2000	Ni II	3455.23	1000	Co I
3132.59	14000	Mo I	3335.20	1800	Ti II	3458.47	5000	Ni I

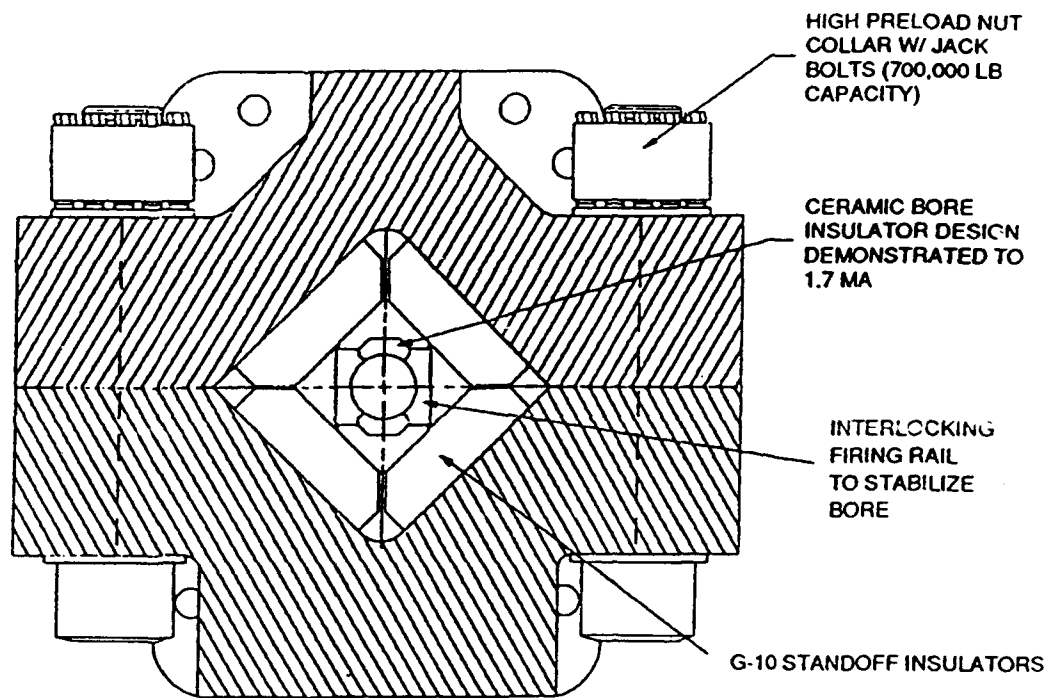


Fig. 1 Cross section of the Thunderbolt Barrel when using the boron nitride insulator.

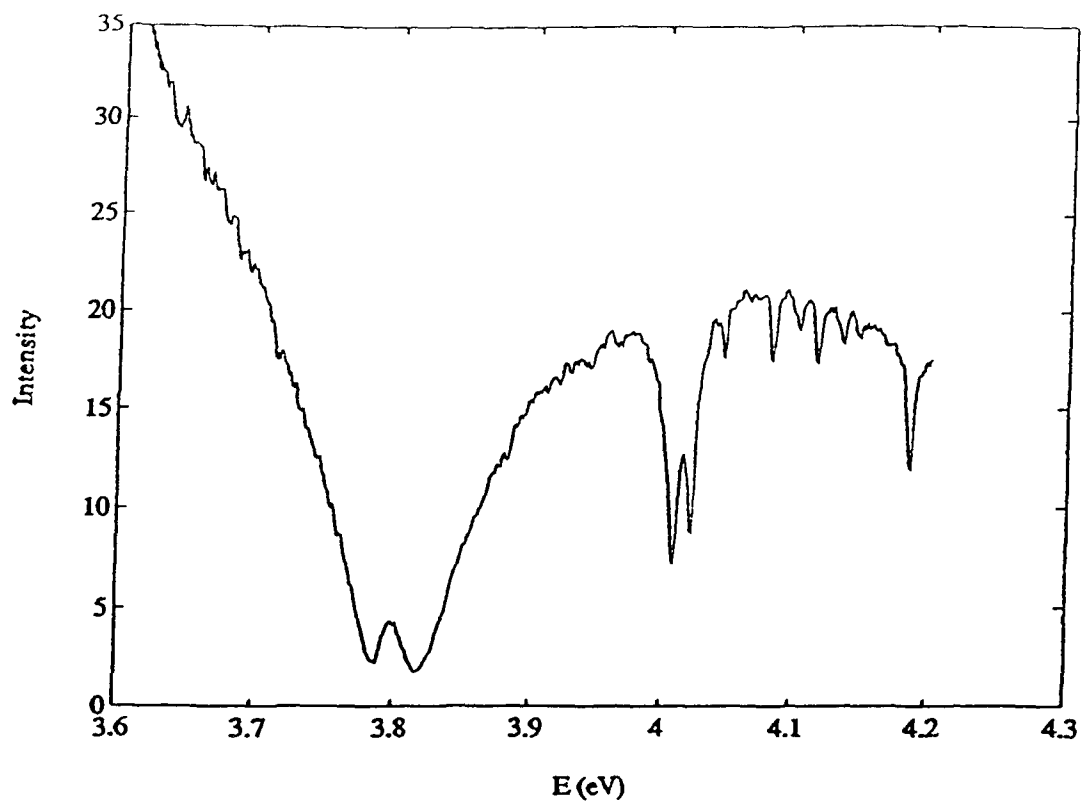


Fig. 2 Experimental Spectrum on Thunderbolt Shot 26.

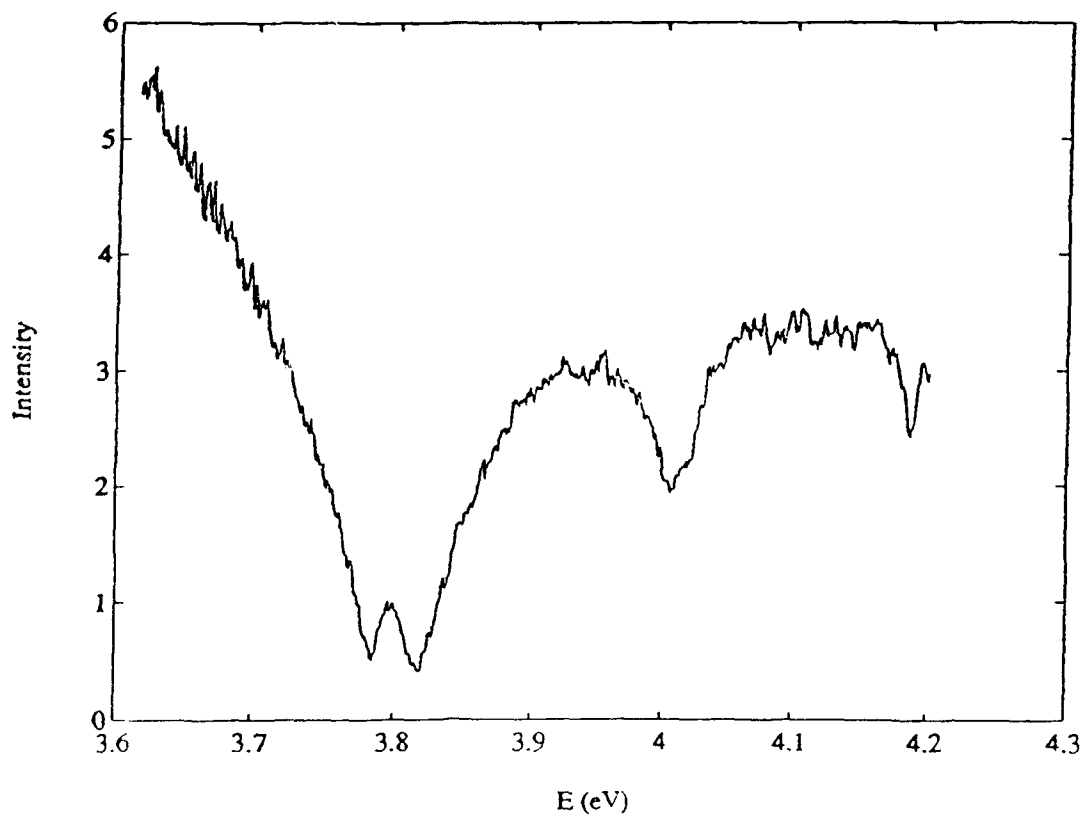


Fig. 3 Experimental Spectrum on Thunderbolt Shot 27.

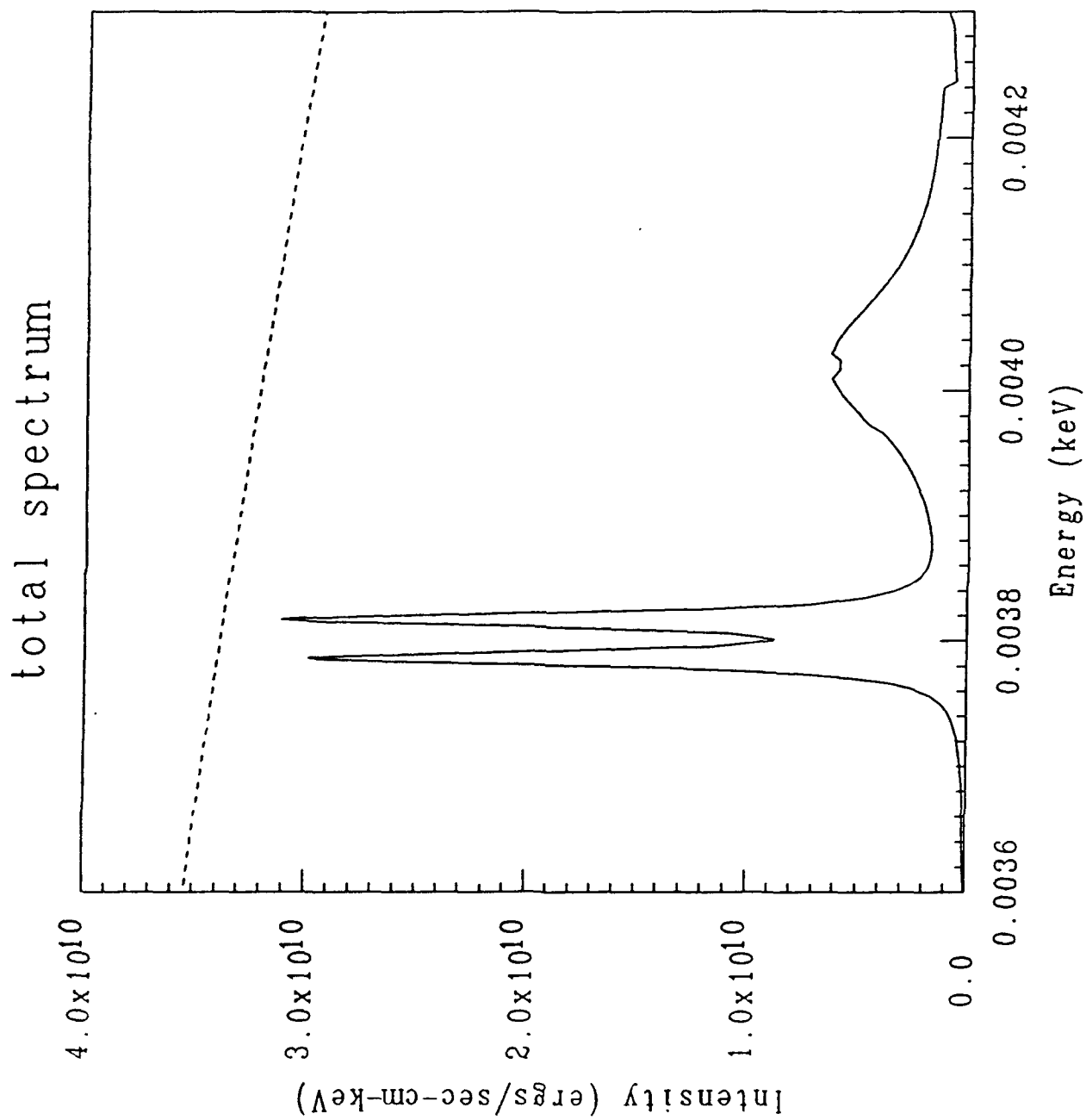


Fig. 4 Optically Thin Spectrum showing two Cu I and one Al I lines. For this run: $P = 3.0 \times 10^8$, $T_c = 1.0$, $\alpha = 0$, Equal number density of Al, Cu, B, and N.

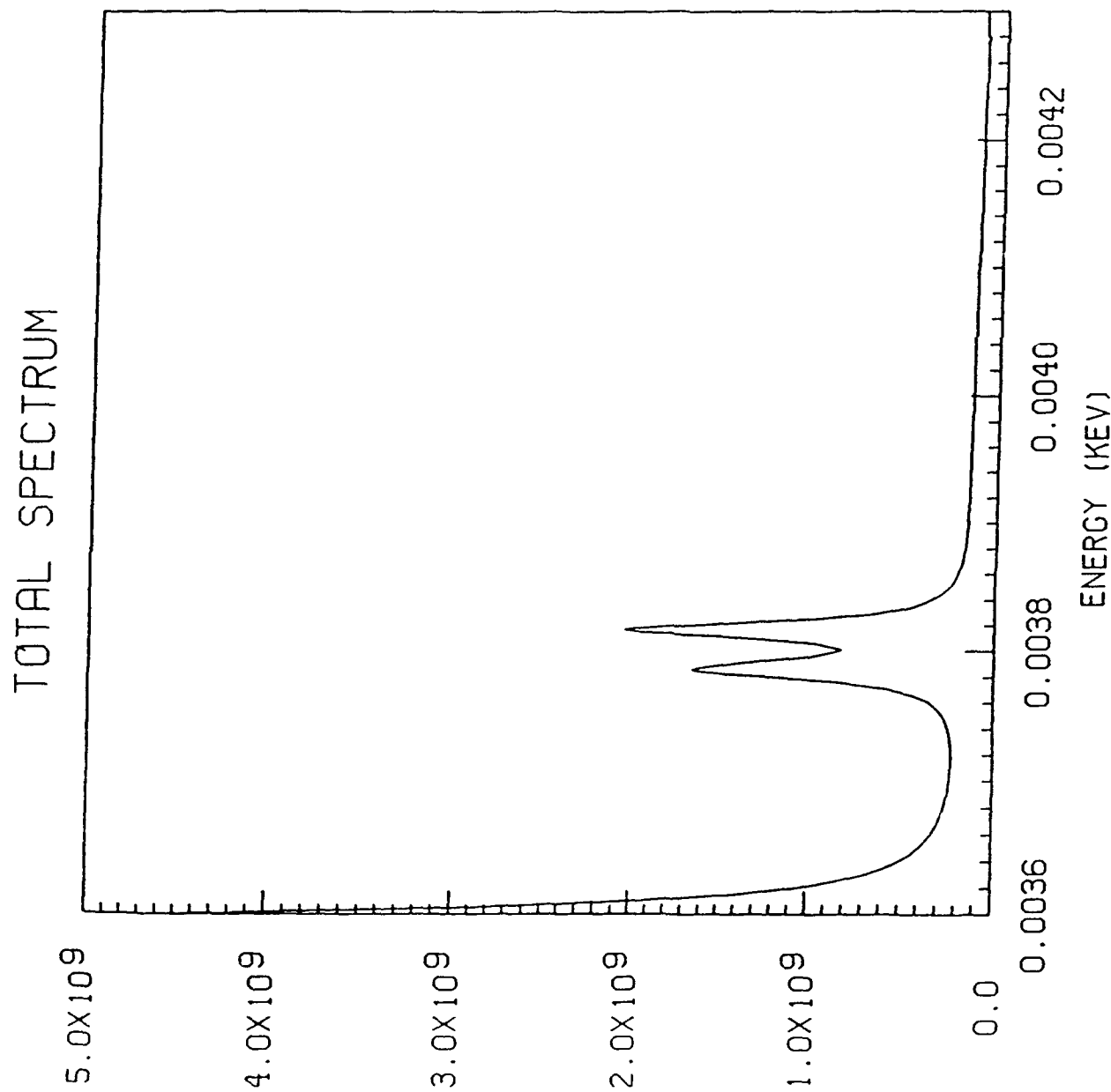
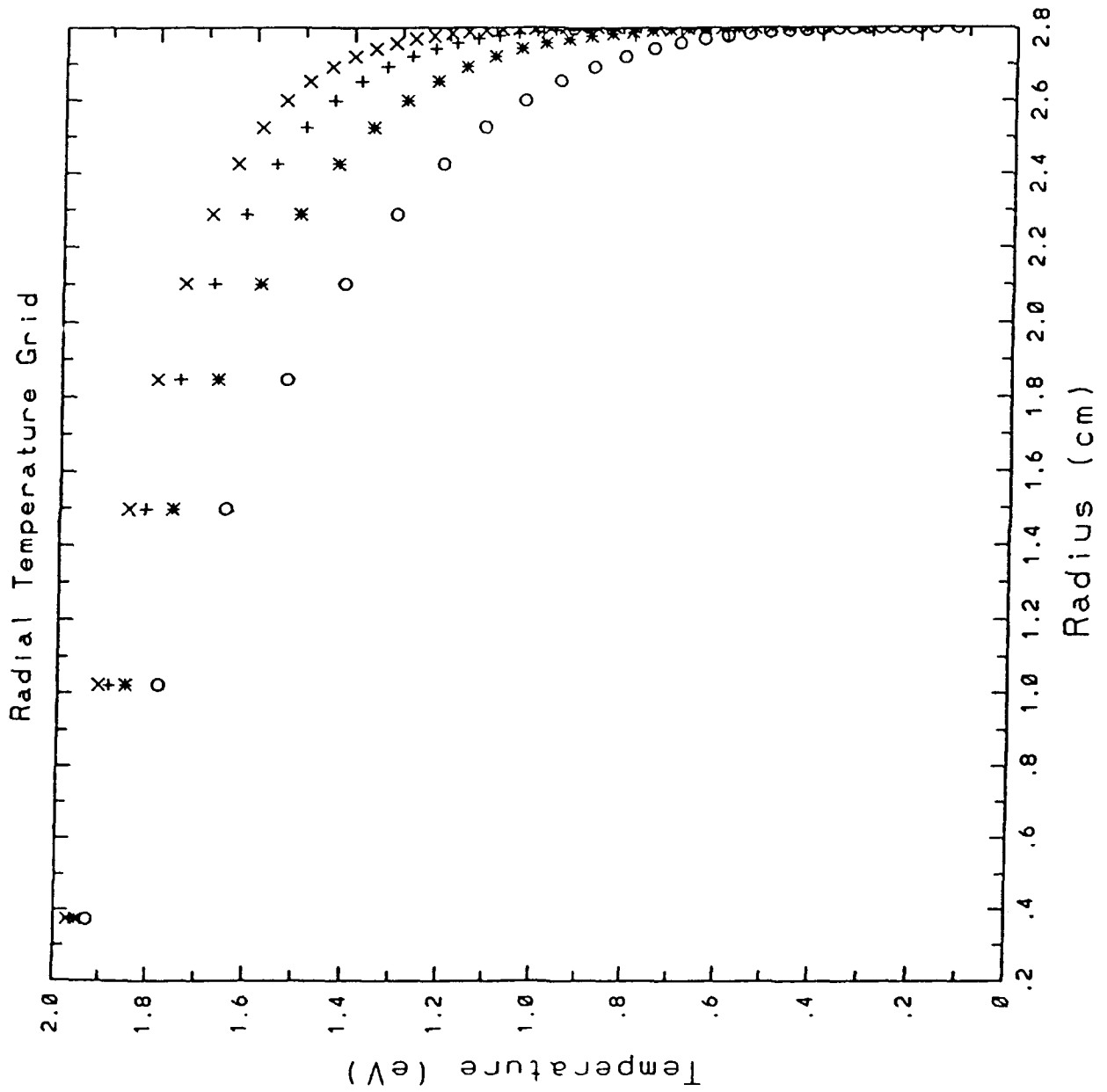


Fig. 5 Optically Thin Spectrum showing the Two Cu I lines and the high energy wing of the B II line. For this run: $P = 3.0 \times 10^8$, $T_c = 2.0$, $\alpha = 0$, % Al = 0.2, % Cu = 20., % BN = 79.8.



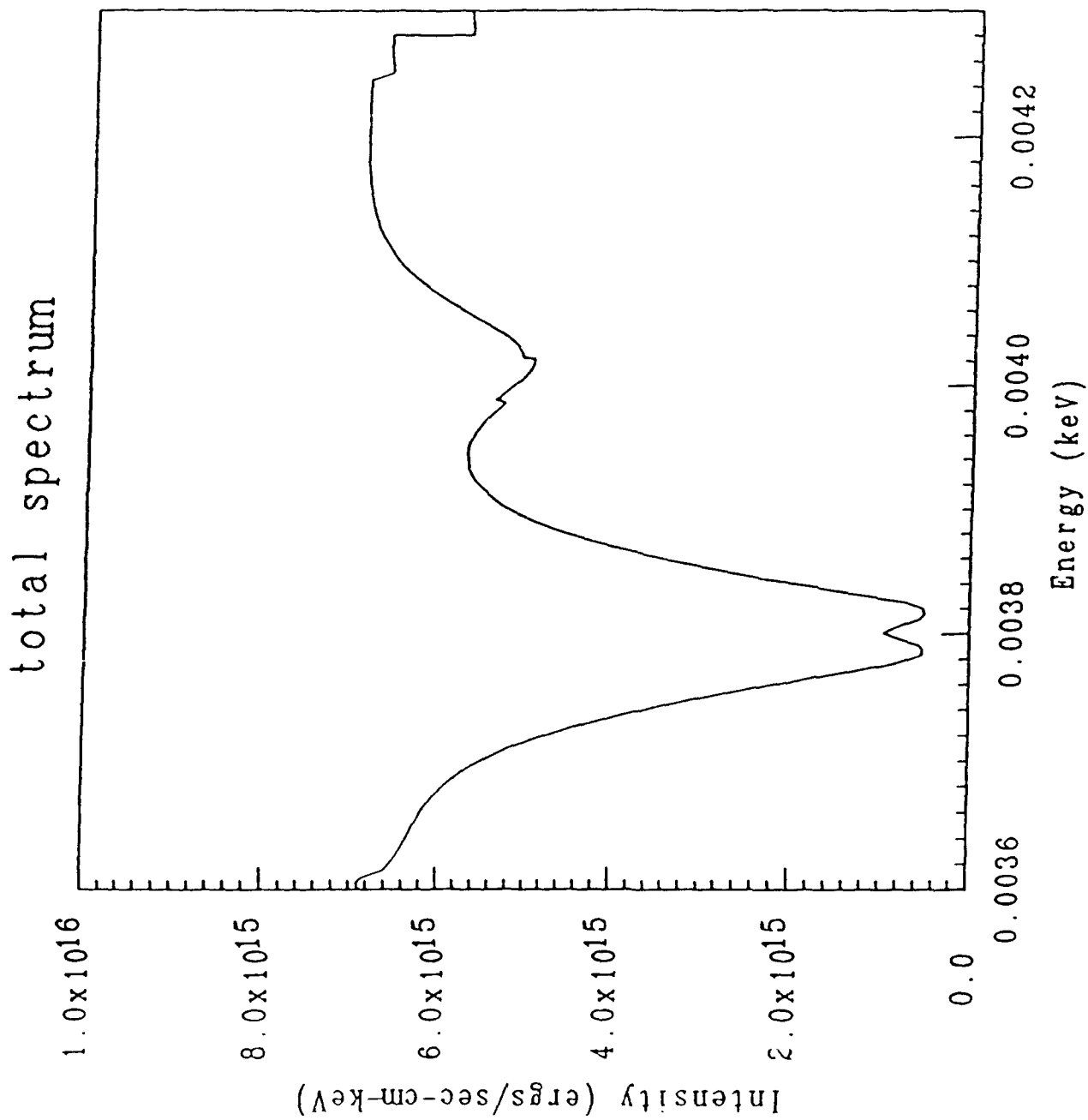


Fig. 7 Theoretical Spectrum. For this run run: $P = 3.0 \times 10^8$, $T_c = 2.0$, $\alpha = 1/10$, % Al = 0.2, % Cu = 20., % BN = 79.8.

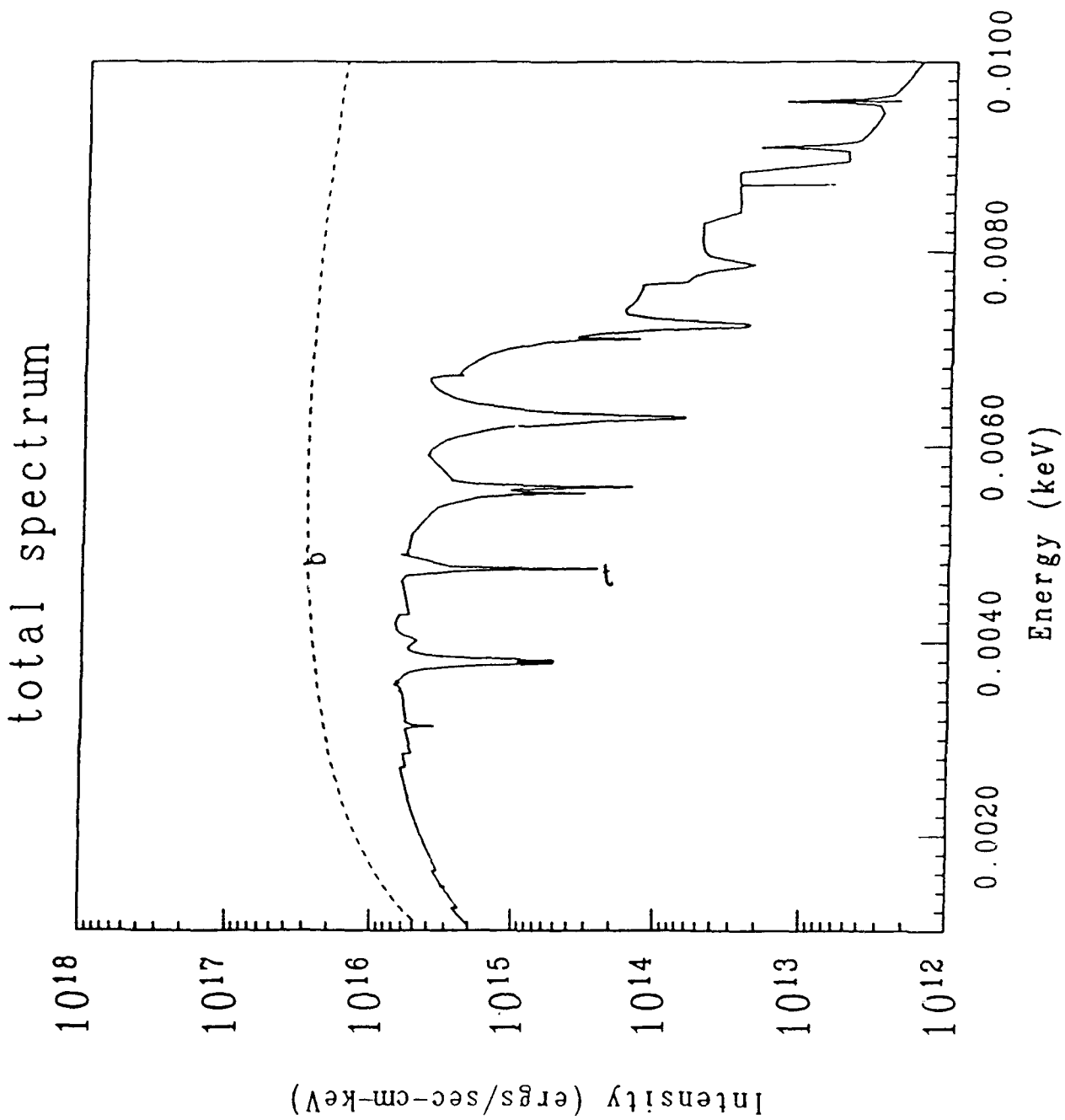


Fig. 8 Theoretical Spectrum. For this run run: $P = 3.0 \times 10^8$, $T_c = 2.0$, $\alpha = 1/10$, % Al = 0.2, % Cu = 20., % BN = 79.8.

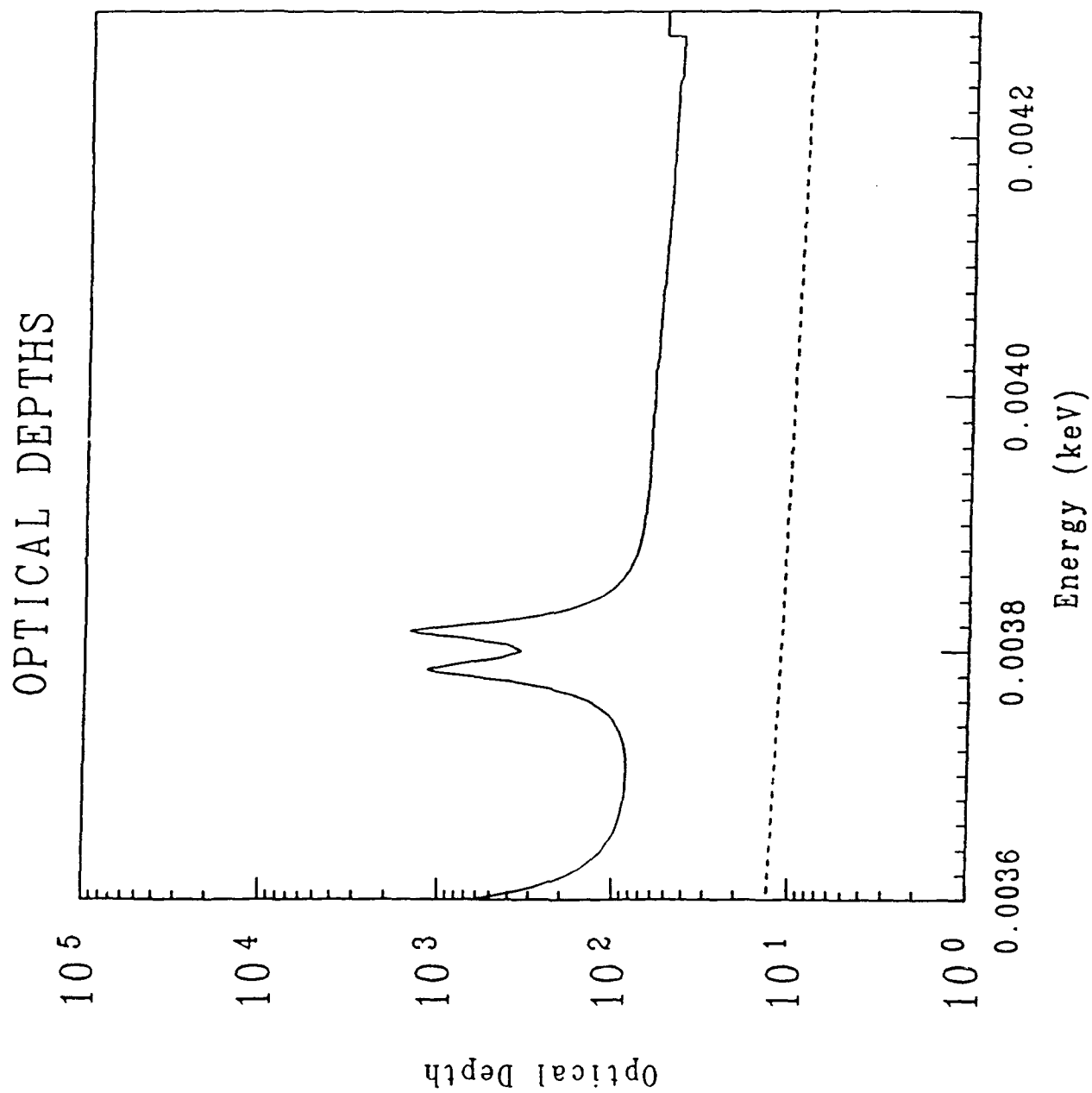


Fig. 9 Optical Depth. Same run as Fig. 7.

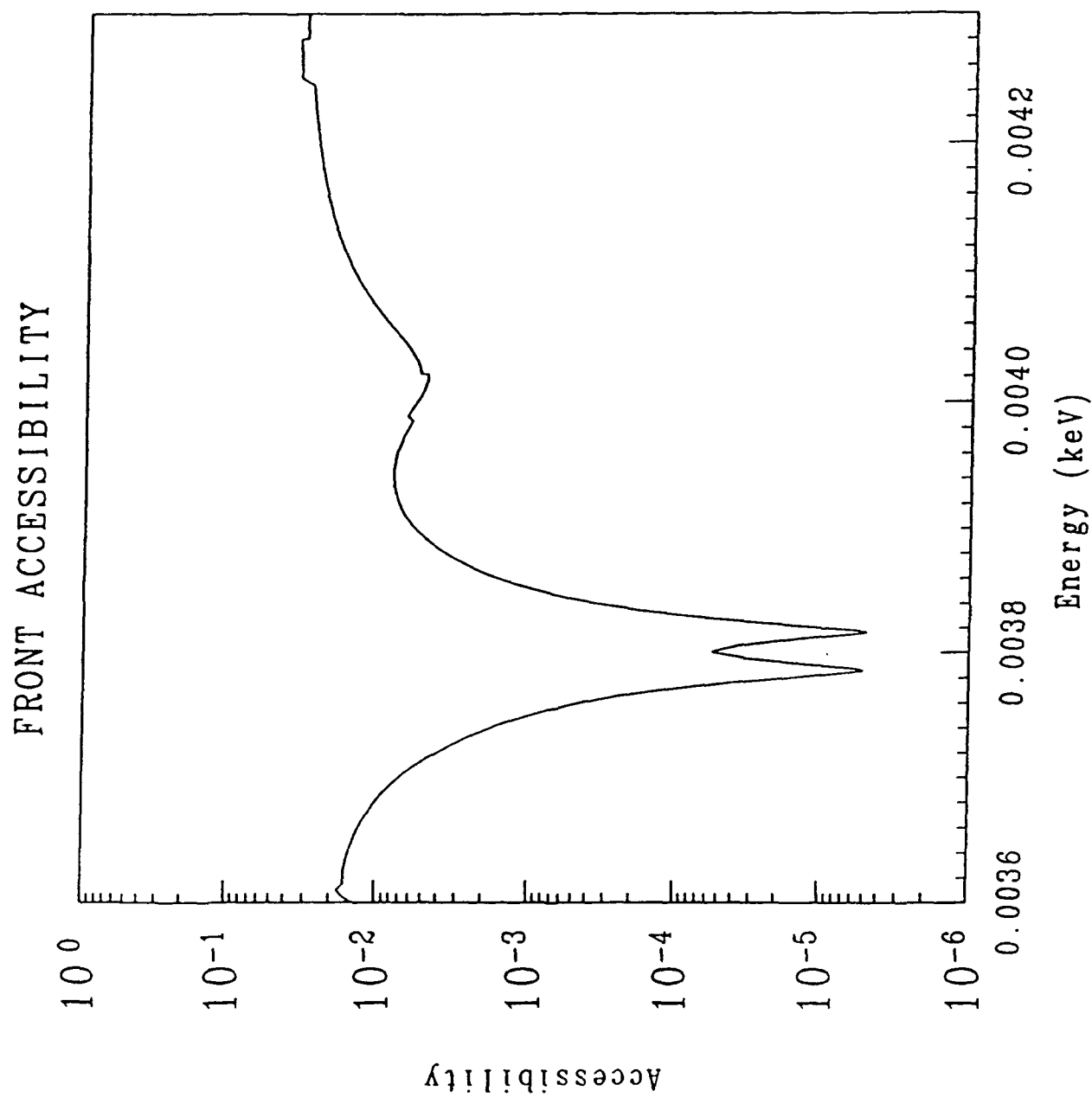


Fig. 10 Front Accessibility. Same run as Fig. 7.

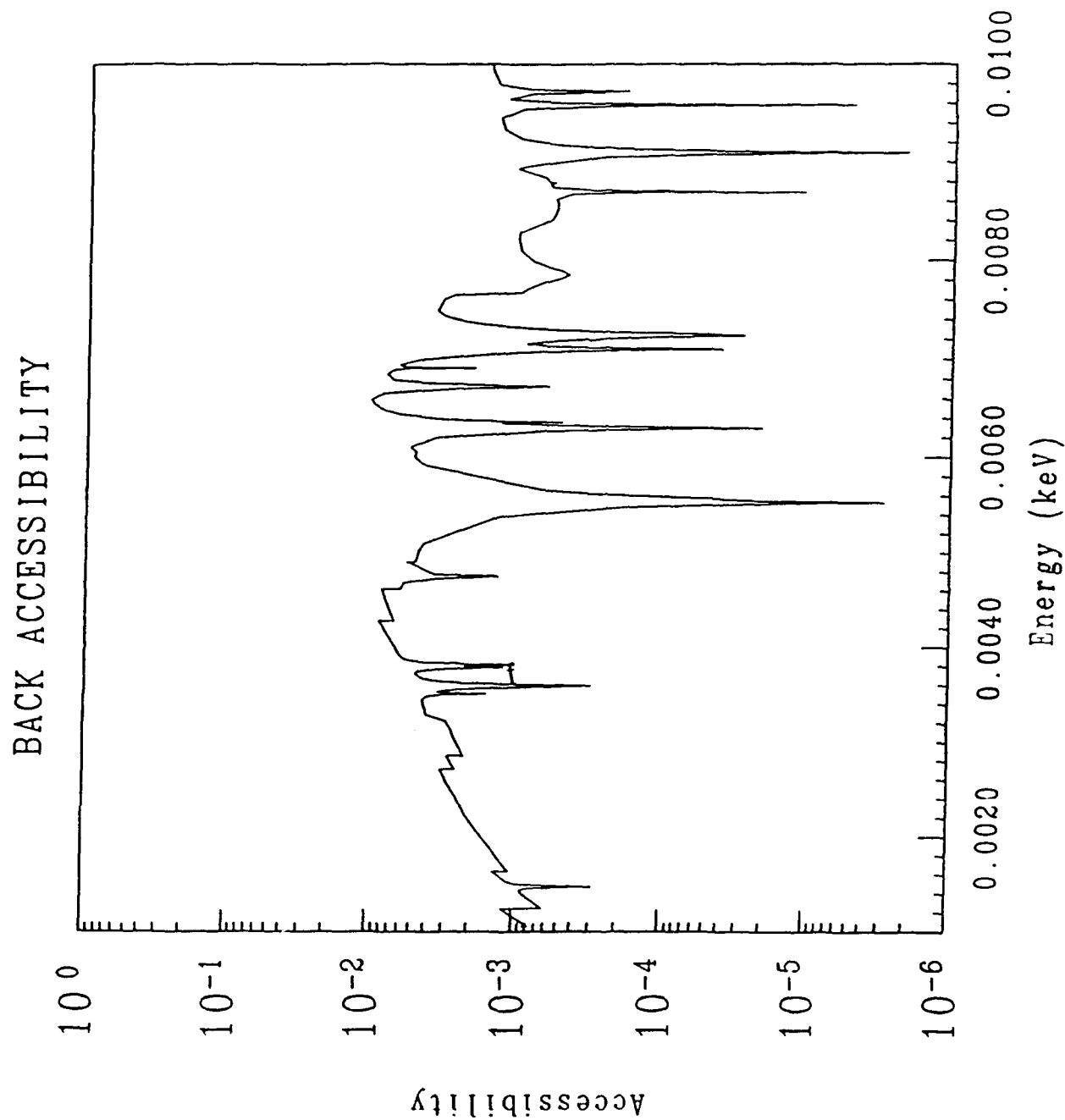


Fig. 11 Back Accessibility. Same run as Fig. 7.

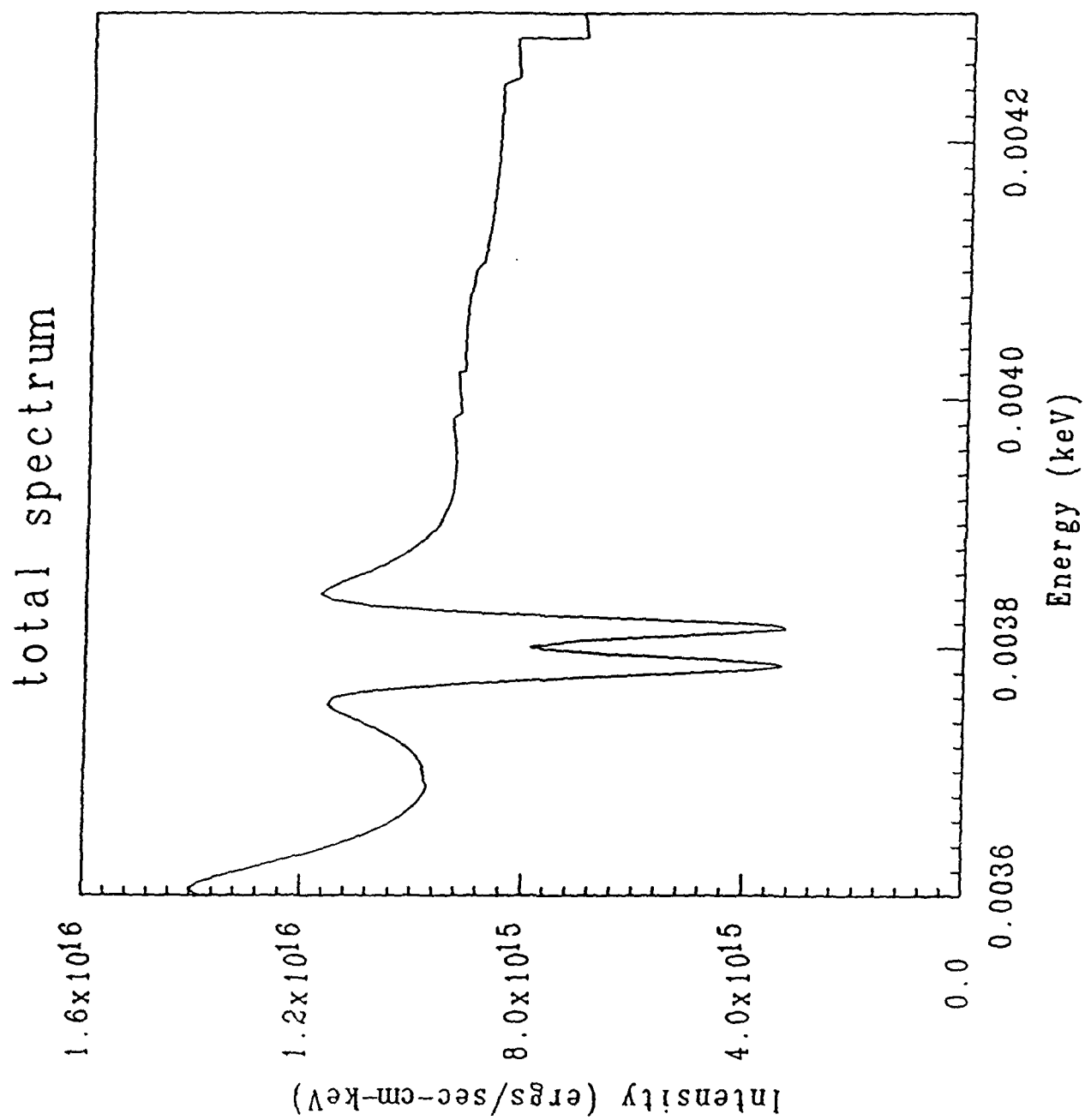


Fig. 12 Theoretical Spectrum. For this run run: $P = 3.0 \times 10^8$, $T_c = 3.0$, $\alpha = 1/10$, % Al = 0.2, % Cu = 20., % BN = 79.8.

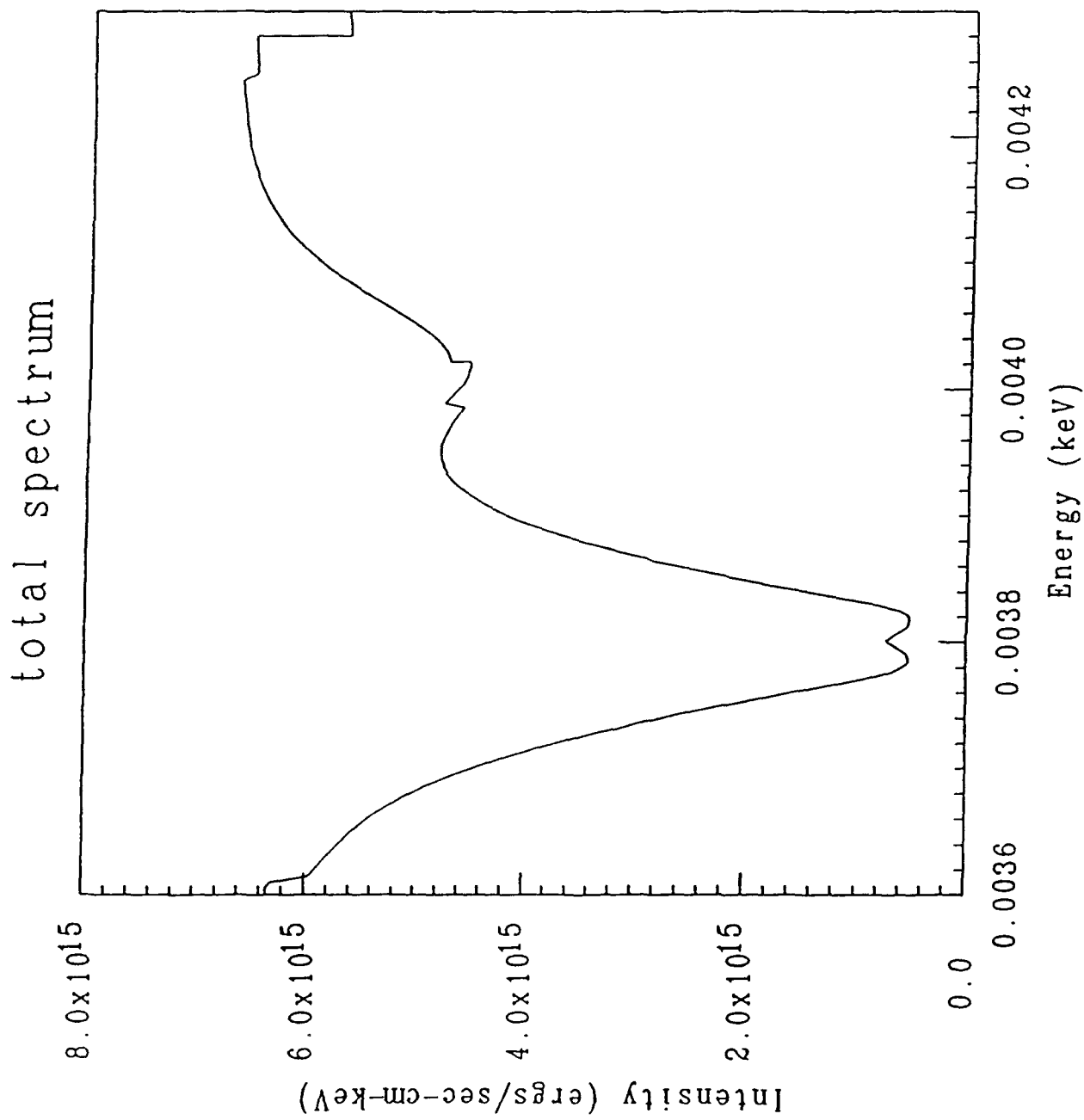


Fig. 13 Theoretical Spectrum. For this run run: $P = 4.0 \times 10^8$, $T_c = 2.0$, $\alpha = 1/10$, % Al = 0.2, % Cu = 20., % BN = 79.8.

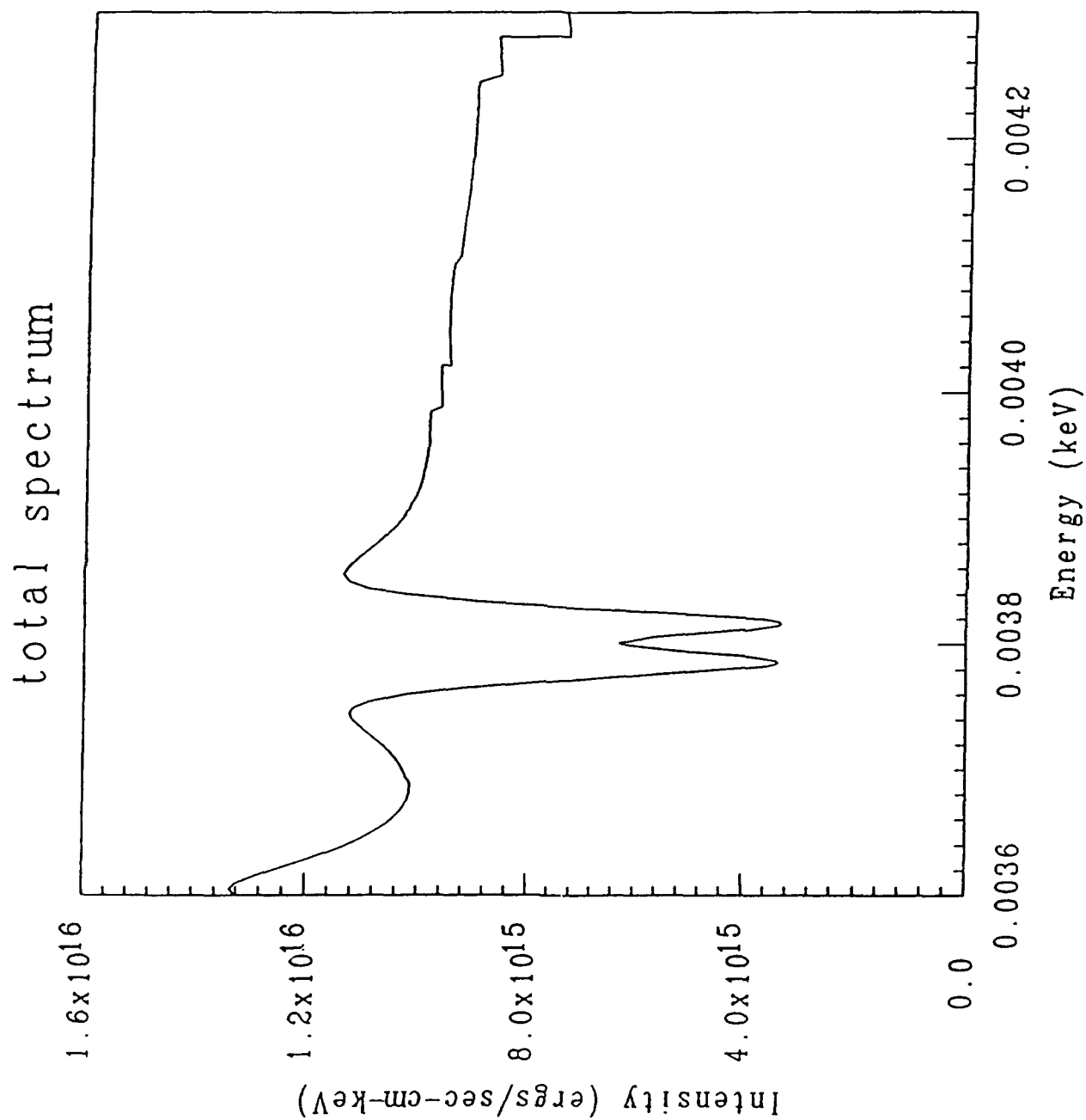


Fig. 14 Theoretical Spectrum. For this run run: $P = 4.0 \times 10^8$, $T_c = 3.0$, $\alpha = 1/10$, % Al = 0.2, % Cu = 20., % BN = 79.8.

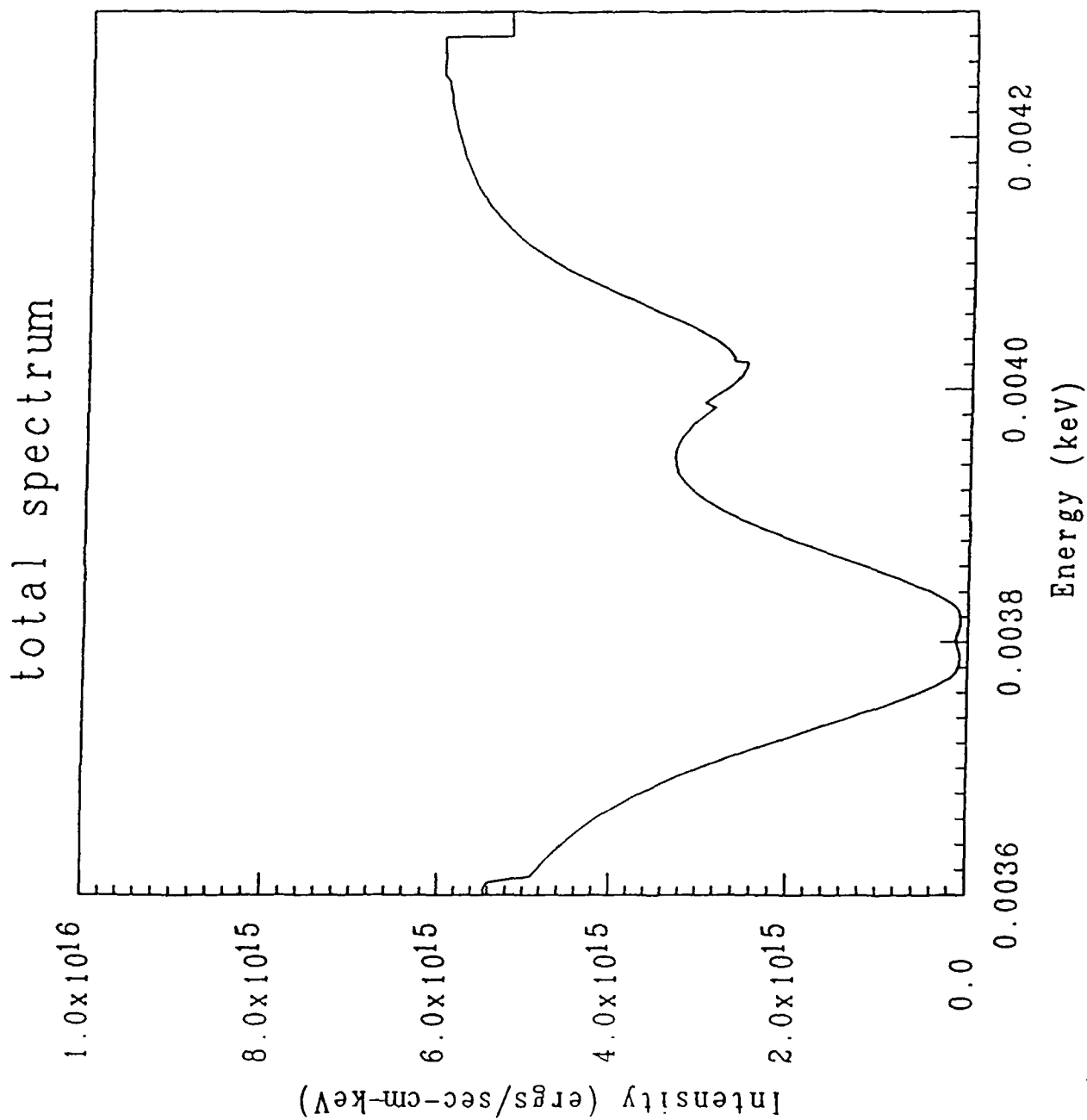


Fig. 15 Theoretical Spectrum. For this run run: $P = 3.0 \times 10^8$, $T_c = 2.0$, $\alpha = 1/8$, % Al = 0.2, % Cu = 20., % BN = 79.8.

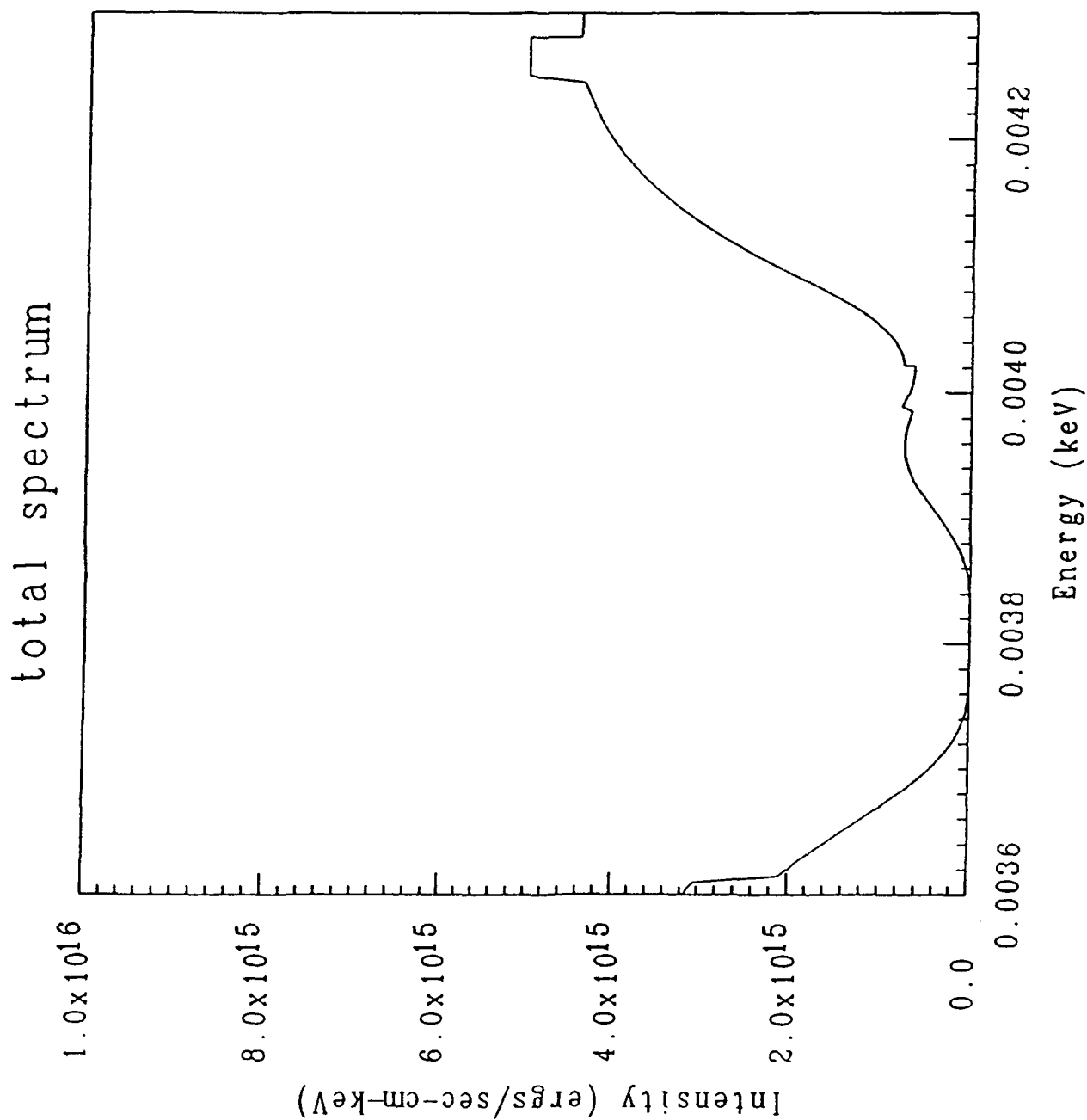


Fig. 16 Theoretical Spectrum. For this run run: $P = 3.0 \times 10^8$, $T_c = 2.0$, $\alpha = 1/6$, % Al = 0.2, % Cu = 20., % BN = 79.8.

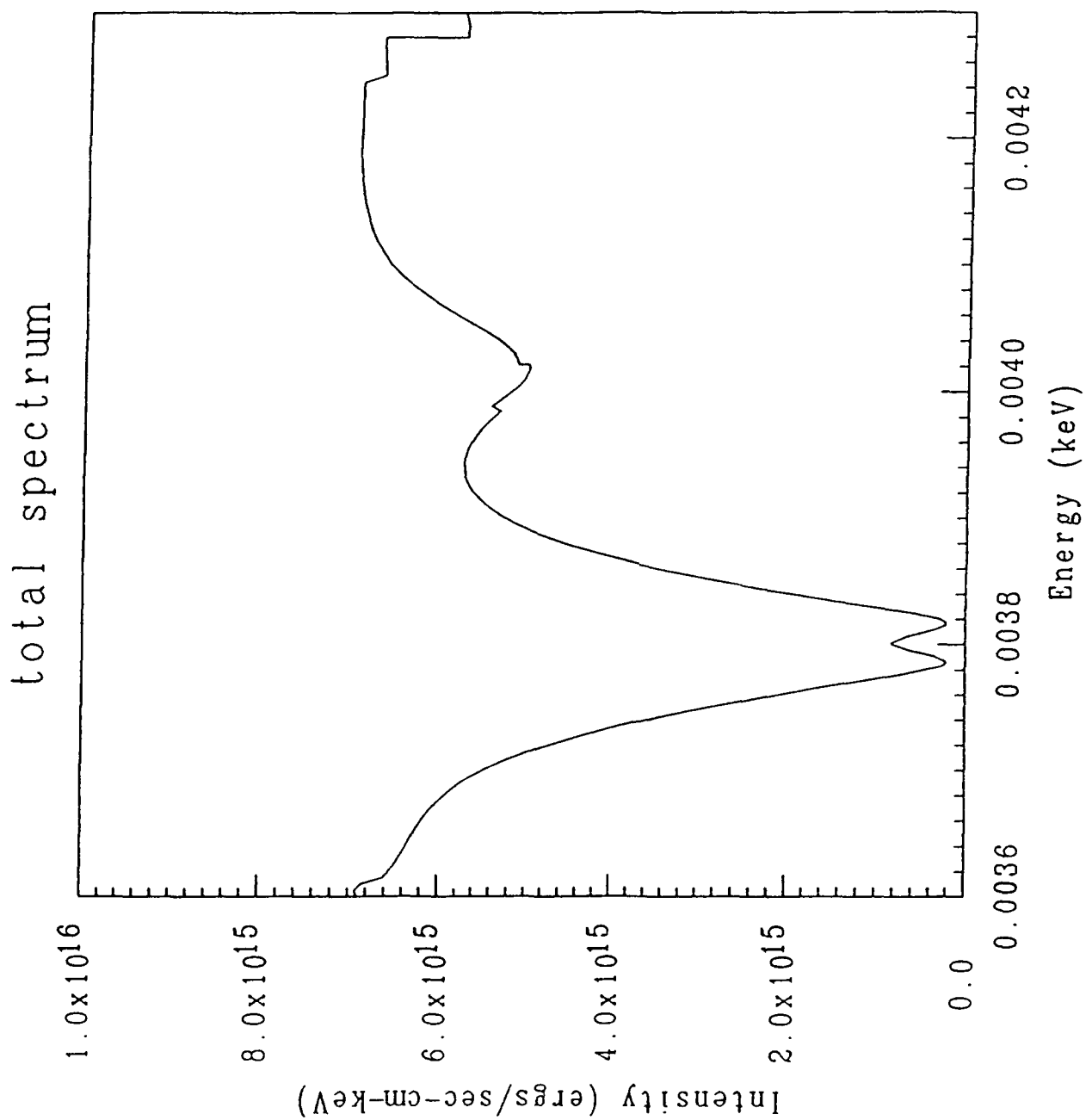


Fig. 17 Theoretical Spectrum. For this run run: $P = 3.0 \times 10^8$, $T_c = 2.0$, $\alpha = 1/10$, % Al = 0.2, % Cu = 20., % BN = 79.8.

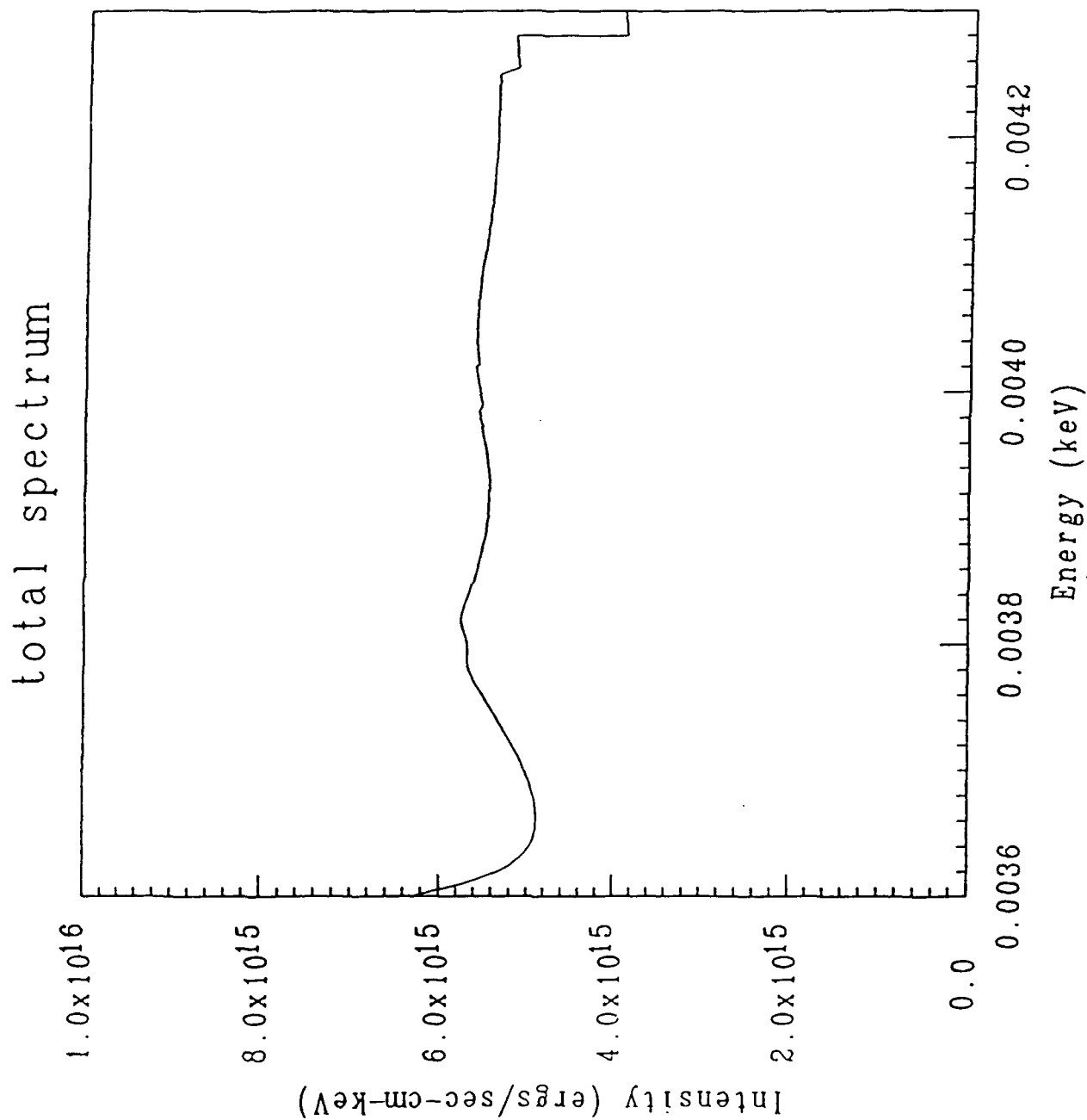


Fig. 18 Theoretical Spectrum. For this run run: $P = 3.0 \times 10^8$, $T_c = 2.0$, $\alpha = 1/10$, % Al = 0.2, % Cu = 20., % BN = 79.8, but with Cu and Al excluded from the outer 1 mm shell.

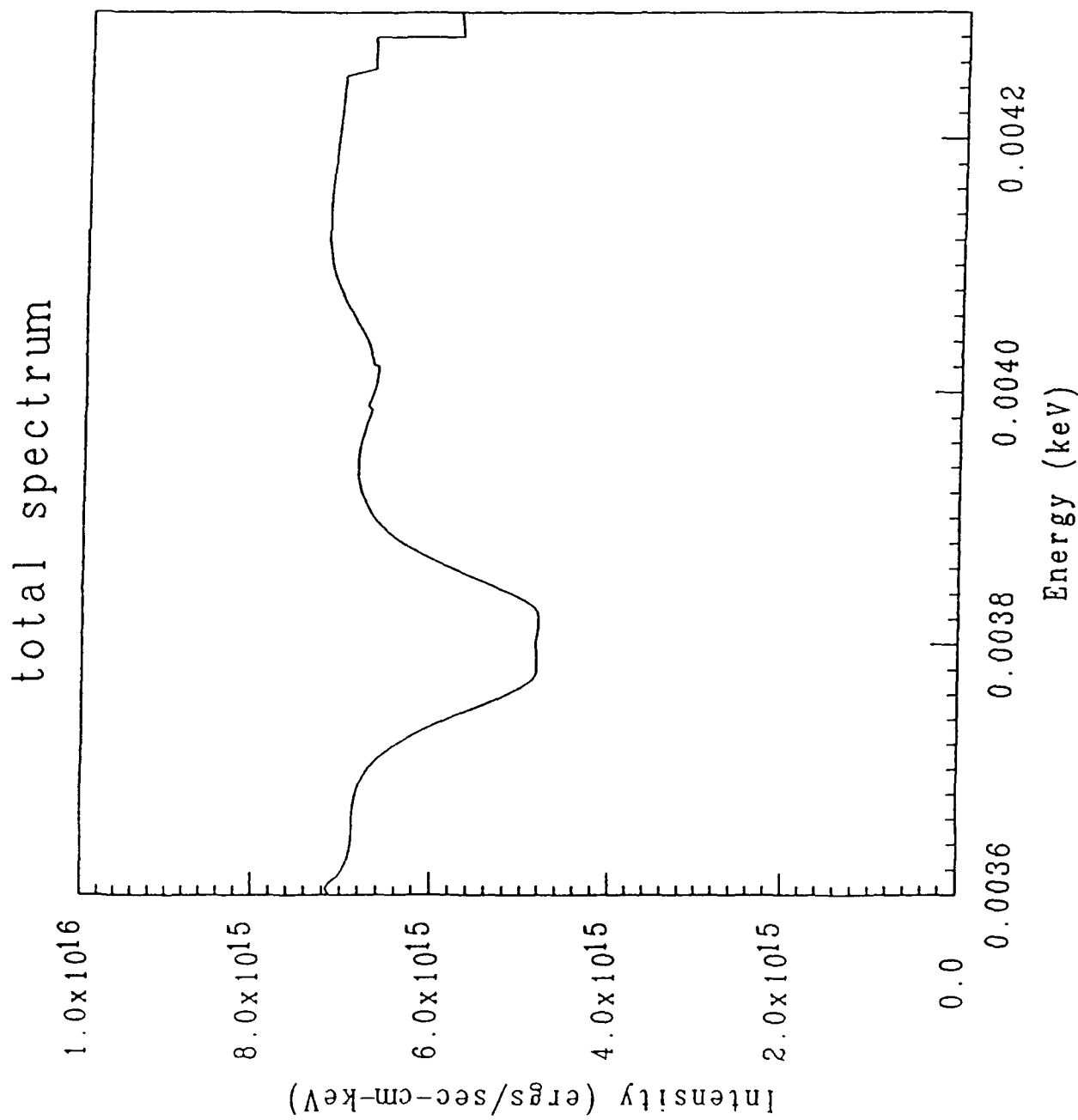


Fig. 19 Theoretical Spectrum. For this run run: $P = 3.0 \times 10^8$, $T_c = 2.0$, $\alpha = 1/10$, $\% \text{ Al} = 0.2$, $\% \text{ Cu} = 20.$, $\% \text{ BN} = 79.8$, but with Cu and Al excluded from the outer 0.07 mm shell.

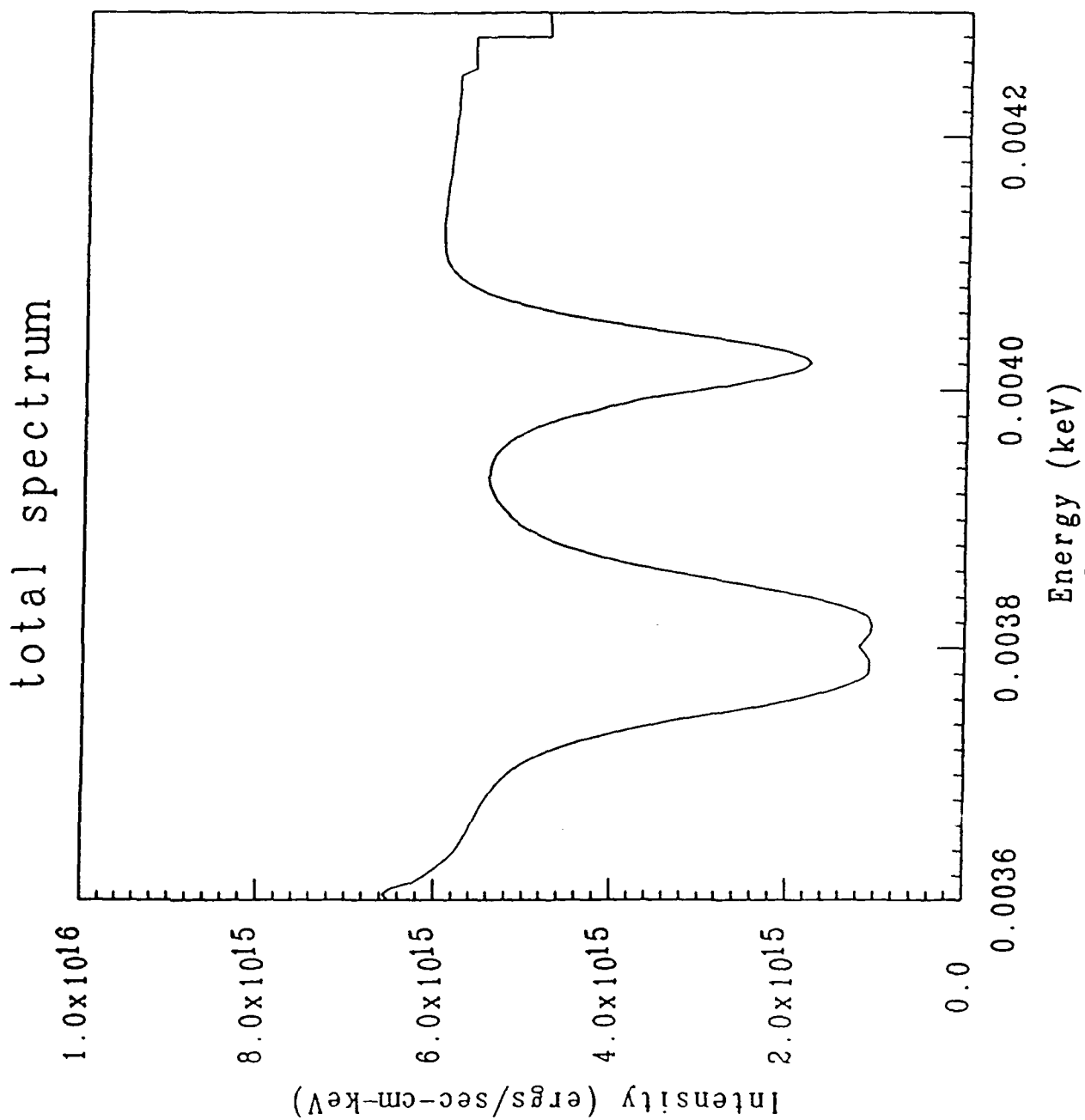


Fig. 21 Theoretical Spectrum. For this run run: $P = 1.0 \times 10^8$, $T_c = 2.0$, $\alpha = 1/6$, % Al = 0.2, % Cu = 20., % BN = 79.8, but with Cu and Al excluded from the outer 0.07 mm shell.

total spectrum

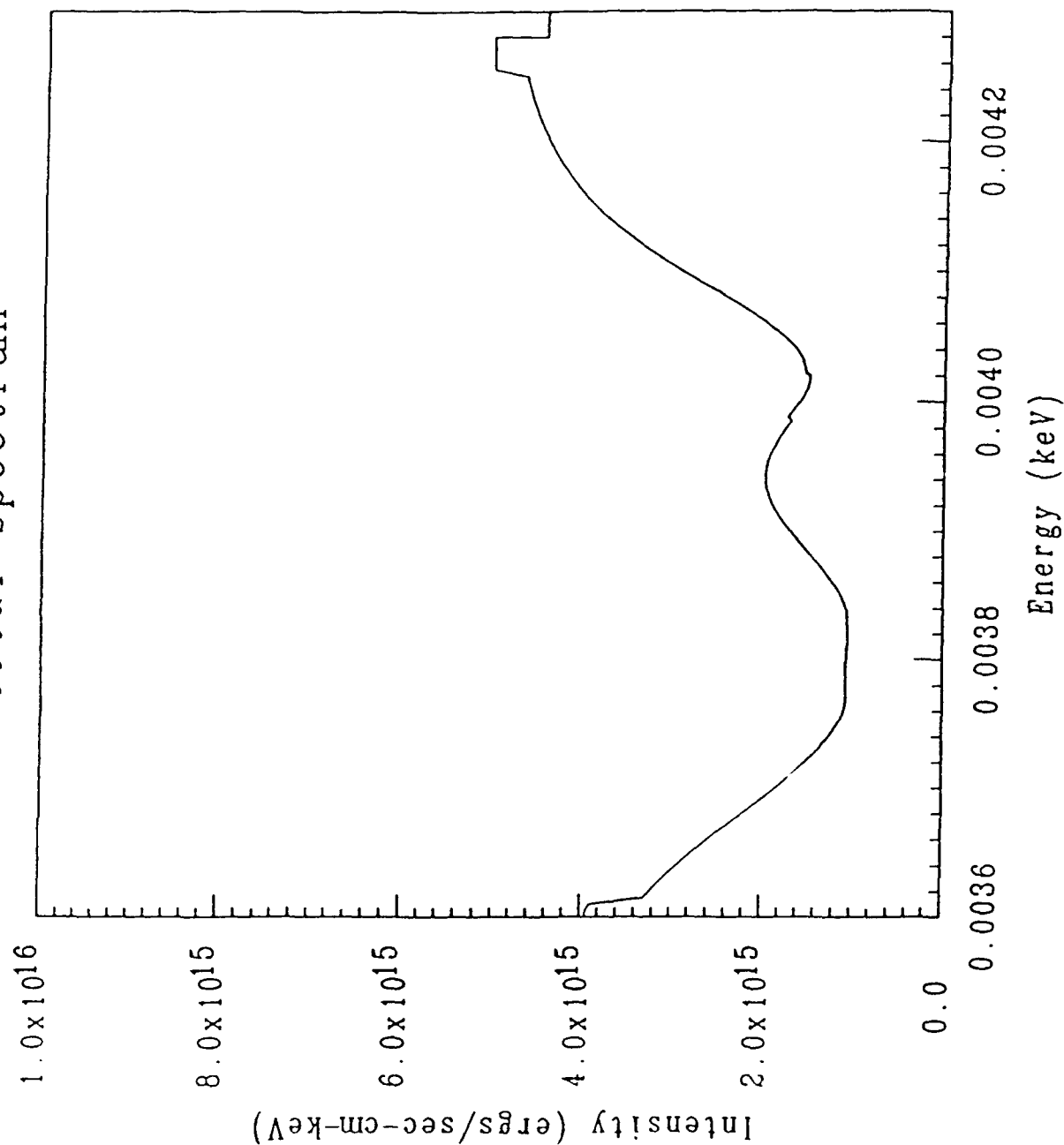


Fig. 20 Theoretical Spectrum. For this run run: $P = 3.0 \times 10^8$, $T_c = 2.0$, $\alpha = 1/6$, % Al = 0.2, % Cu = 20., % BN = 79.8, but with Cu and Al excluded from the outer 0.07 mm shell.